VRIJE
UNIVERSITEIT
BRUSSEL

Master thesis submitted in partial fulfilment of the requirements for the degree of
Master of Science In de Ingenieurswetenschappen: Computerwetenschappen

VARIATIONAL GREEDY INFOMAX

Interpretable representation learning with latent space constraints

Fabian Denoodt

2022-2023

Promotor(s): Prof. Dr. Bart de Boer

Science and Bio-Engineering Sciences

VRIJE
UNIVERSITEIT
BRUSSEL

Proefschrift ingediend met het oog op het behalen van de graad van Master of Science In de Ingenieurswetenschappen: Computerwetenschappen

VARIATIONAL GREEDY INFOMAX

Interpreteerbare representaties leren met beperkingen van de latente ruimte

Fabian Denoodt

2022-2023

Promotor(s): Prof. Dr. Bart de Boer

Wetenschappen en Bio-ingenieurswetenschappen

Abstract

This thesis introduces Variational Greedy InfoMax (V-GIM), a self-supervised representation learning method that incorporates an interpretability constraint into both the network and the loss function. V-GIM's architecture is split up into modules, each individually optimised to promote interpretability by imposing constraints on their respective latent spaces. This approach enables the analysis of the underlying structures in the internal and final representations.

Inspired by Variational Autoencoders (VAE), V-GIM represents each module's representations as samples from Gaussian distributions. These representations are optimised to maximise the mutual information between temporally nearby patches using the InfoNCE bound introduced in (van den Oord et al., 2019). However, V-GIM introduces a regularisation term to the loss function, encouraging distributions to approximate the standard normal distribution, thereby constraining the latent space of each module. By enforcing these latent space constraints, V-GIM ensures that sampling a random point from the standard normal distribution within a specific latent space is likely to correspond to a meaningful data point in the original space, similar to the points in the dataset. This constraint also promotes smooth transitions in the latent space with respect to the mutual information. V-GIM's latent space is utilised to train a decoder, enabling the analysis of the underlying structure of representations at different levels in the architecture while ensuring good generalisation. Additionally, we argue that V-GIM's latent space constraint is related to theories from VAEs leading to disentangled representations, which could potentially enable easier analysis of the model through post-hoc explainability approaches.

We evaluate V-GIM's performance on sequential speech data. V-GIM achieves similar performance to its less interpretable counterpart, GIM, and even outperforms it in deeper modules due to V-GIM's internal batch normalisation mechanism. We examine the potential of V-GIM's representation variance as a data augmentation tool for downstream tasks with limited labelled data and demonstrate that the variability in representations does not contribute to improved performance. Finally, we provide insights into V-GIM's internal representations. We demonstrate that the representations learn to differentiate between vowel information while consonant information appears to be less prominent. Additionally, we discuss which internal neurons are sensitive to which vowels, further demonstrating the interpretability of V-GIM.

Our code is available via GitHub.

Preface

I am proud to share with you the final milestone of my academic journey as a Computer Science student, specialised in Artificial Intelligence at Vrije Universiteit Brussel. As you will see, this thesis heavily relies on mathematics. Ironically, in high school, I used to struggle with mathematics and tried to avoid it whenever possible. That is why I pursued a professional bachelor's degree in Applied Information Technology at a college that did not include any mathematics courses. However, during my bachelor's, I gained a strong interest in machine learning. The idea of a computer learning to perform tasks without explicit instructions fascinated me. But to delve deeper into this field, I realised I needed to catch up on my weak mathematics background. It was a major challenge for me, but slowly and steadily, I began to grasp the concepts and even found myself enjoying it. Despite initially feeling overwhelmed, each "aha" moment brought a sense of satisfaction that made me appreciate mathematics more and more. Today, I can proudly say that I have overcome this challenge, resulting in this thesis on representation learning with latent space constraints.

I couldn't have come this far without the support of those around me. I am immensely grateful to Prof. Dr. Bart de Boer, my thesis supervisor, for his guidance and engaging discussions. Despite my ever-changing ideas, he steered me towards a focused topic while encouraging my creativity and providing realistic feedback. I would also like to express my gratitude to Prof. Dr. Bart Dhoedt, who taught the Deep Generative Models course at UGent. Your course and the interesting discussions we had, have given me great insights, ultimately improving the quality of my thesis. Thank you to my parents for their continuous support. Lastly, I want to acknowledge the creators of OpenAI. Ironically, this thesis is not only about AI but is also partly written with the assistance of AI. ChatGPT, in particular, served as an advanced grammar checker and contributed to stylistic improvements throughout this work.

Contents

Chapter 1

Introduction

1.1 Motivations

Black-box models have shown incredible performance in recent years. Notable breakthroughs include AlphaGo defeating the world champion Go player in 2016 (Fu, 2016), and ChatGPT, which can assist with coding, reason through problems and generate well-written documents.

These models are typically trained using deep neural networks in an end-to-end fashion. Despite their impressive success, their lack of interpretability poses a significant challenge. The internal workings of these models are often not well understood, limiting their applicability in high-stakes decision-making scenarios, such as medical diagnosis, law or defence. A simple binary answer does not suffice; we need to ensure these models make decisions for the right reasons (Alammar, 2021). Additionally, a comprehensive understanding of these models is essential if humans wish to learn from them, for instance by applying strategies similar to those learned by AlphaGo.

While models that are interpretable by design do exist (e.g., logistic regression, linear classifiers and decision trees), they are limited by their simplicity and are not always able to model the complex problems in our world. Therefore, for certain problems, more complex models are required which results in reduced interpretability. To gain a better understanding of these less interpretable models, various post-hoc approaches have been explored. These approaches aim to find explanations for models that are not interpretable by design, for instance through techniques such as visual explanations, text explanations and feature attribution explanations (Barredo Arrieta et al., 2020). We focus on feature attribution techniques. Some techniques include LIME, SHAP, and gradient-based methods, which compute a relevance or contribution score for each input feature with respect to the output prediction (Simonyan et al., 2014; Ribeiro et al., 2016; Lundberg and Lee, 2017; Molnar, 2022). These approaches are frequently used for image classification via heatmaps, highlighting the important pixels that had the largest contribution to the decision.

Although these post-hoc approaches provide some insights into what the important key factors are that led to an individual prediction, they do not say much about the internal workings of the model. Particularly, in artificial neural networks (ANN), it is known that specific neurons are sensitive to particular concepts. Zeiler and Fergus (2013) show that the initial layers in Convolutional Neural Networks (ConvNets) trained for image classification, learn to recognise abstract concepts such as lines and edges, while deeper layers learn more semantically meaningful concepts such as the shape of a nose or ear, without being explicitly told to do so. Continuing in the line of post-hoc approaches, multiple explainability methods have been investigated that analyse

the internal neurons, resulting in an improved understanding of the underlying mechanisms of these ANNs. Notable contributions aim to find the image that maximally activates a specific neuron (Simonyan et al., 2014) (or, equivalently, a channel in a ConvNet). A second approach aims to, highlight the regions of an image that a particular neuron is sensitive to (Zeiler and Fergus, 2013).

However, many approaches that aim to analyse individual neurons focus on images, as their explanations are more easily interpretable. Conversely, when it comes to input features that are less visually interpretable, such as raw speech signals, utilising these explainability methods may be impractical for such models (Krug et al., 2021). Moreover, Bau et al. (2017) argue that the internal semantic concepts learned by these neurons are highly entangled throughout the network. This makes interpretation of neurons particularly difficult, as multiple neurons may work as a whole and together be sensitive for a semantic concept such as a nose (Molnar, 2022). Therefore, there may not always be an individual neuron that is responsible for a specific concept, and these concept-sensitive neurons may even span multiple layers, further complicating the analysis of these black-box models.

We argue that these concerns regarding interpretability are especially relevant in representation learning. Neurons in the network learn semantic concepts of the data, and their activations at a particular layer can potentially serve as an alternative representation for the data. This process of learning new representations for data is known as representation learning (Le-Khac et al., 2020). These representations then serve as the inputs for downstream tasks such as classification or regression. However, in order to ensure that these downstream tasks make meaningful predictions, we must make sure that the representations they are trained on contain meaningful information. Therefore, a good understanding of the representations is needed.

1.2 Main Research Question

Given the entangled nature from these black-box models, it is likely impossible to fully understand them using solely post-hoc techniques. Therefore, in this thesis we aim to incorporate interpretability requirements into the design of the model instead. By enforcing additional constraints to the loss function, such as disentanglement, we could potentially improve the interpretability of these ANNs, thereby improving the effectiveness of these post-hoc explanations while maintaining good performance.

In representation learning, a well-known approach is the Variational Autoencoder (VAE). VAEs indirectly encourage interpretable representations by imposing additional constraints to the space of plausible representations, commonly referred to as the *latent space* (Kingma and Welling, 2022). Additionally, recent work has shown that the latent space constraint in VAEs encourages disentangled representations, further improving upon interpretability (Burgess et al., 2018; Sikka et al., 2019; Higgins et al., 2022).

Contrastive methods are another representation learning framework that have seen interest in recent years, learning representations for data by discriminating them against noise (Chen et al., 2020). In particular, we focus on the information maximisation approach introduced by van den Oord et al. (2019) in Contrastive Predictive Coding (CPC), which learns representations for sequential data by predicting the representations of future observations given those from the past Henaff (2020). CPC has demonstrated remarkable success in a wide range of domains and is currently considered the state-of-the-art method for representation learning from sequential data without labels (Stacke et al., 2020; de Haan and Löwe, 2021; Lu et al., 2019; Bhati et al., 2021; Deldari et al., 2021; Henaff, 2020). However, CPC does not directly include an interpretability aspect to its representations, and the underlying representations obtained by optimising the

InfoNCE objective in CPC have not been thoroughly studied.

To address these challenges, we introduce Variational Greedy InfoMax (V-GIM), a representation learning framework that learns interpretable representations by enforcing constraints on the latent space. Derived from Löwe et al. (2020), V-GIM splits the architecture into modules, each trained greedily using a novel loss function that promotes interpretable representations. We introduce a post-hoc explainability approach via a decoder which utilises the constrained space to ensure meaningful decodings. This allows for the analysis of neurons at different depths in the architecture, enhancing interpretability for both the final and internal representations. In this thesis, we examine V-GIM's performance and analyse the interpretability of its learned representations, with a focus on raw speech waves.

Our contributions are the following:

- We introduce V-GIM and demonstrate that it enables a better understanding of the learned representations, allowing for the observation of information in individual neurons, both in the final and internal representations.
- We show that V-GIM offers computational benefits, including internal batch normalisation, and outperforms its less interpretable counterpart GIM in certain cases. Additionally, we examine V-GIM's stochastic representations, potentially serving as a data augmentation tool for downstream tasks with little labelled data.
- We apply a range of techniques, including a decoder that takes into account human perception biases when listening to audio, gaining insights into V-GIM's learned representations. Through this analysis, we make suggestions on which data is incorporated in which neuron and which information may no longer be present in the representations.

The structure of this thesis is as follows: in chapter 2, we provide an overview of the necessary background information needed to fully understand our work, which is described in chapter 3. In chapter 4, we examine the performance of V-GIM compared to its non-variational counterpart GIM and provide an analysis of the learned representations. Chapter 5 presents a literature review of related work and compares it to V-GIM. Finally, in chapter 6 we conclude this thesis with a discussion on V-GIM's main findings and make suggestions for future work.[1].

[1]The structure of this thesis is based on Sindy Löwe's master's thesis in Artificial Intelligence from the University of Amsterdam.

Chapter 2

Background

Our proposed approach, V-GIM, aims to obtain the state-of-the-art performance obtained from GIM while leveraging the interpretability obtained from Variational Autoencoders (VAE). We achieve this by combining ideas from both methods into a single framework. In this section, we discuss the necessary background required to understand these concepts, as they will set the basis for our own contribution. We commence by addressing the challenges in supervised machine learning with respect to generalisation and make motivations on how representation learning can address these issues. We then give a short intermezzo on information theory, which will be relevant for understanding the information-theoretic motivations in CPC and VAEs.

2.1 Artificial Neural Networks and Generalisation

Machine learning considers the problem of programming a computer via data, rather than explicit code instructions. In particular, in supervised machine learning, we may be interested in finding a mapping function $f(\cdot)$ that can infer a label $\mathbf{y}^{(i)} \in \mathcal{Y}$ given an observation or *feature vector* $\mathbf{x}^{(i)} \in \mathcal{X}$. The function $f(\cdot)$ can then be denoted as follows:

$$f : \mathcal{X} \to \mathcal{Y}$$

Different approaches exist on representing this function. Some examples include decision trees, support vector machines and Artificial Neural Networks (ANN). In the next section, we will focus on how this is achieved through ANNs.

2.1.1 Fully Connected Neural Networks

Artificial Neural Networks (ANNs) are parametric, non-linear learning functions (Löwe et al., 2020) that can be represented as a set of $1 \dots L$ layers. Each layer l consists of a transformation matrix $\mathbf{W}^l$ and a non-linearity function $\sigma(\cdot)$ (Jain et al., 1996; Krogh, 2008; Zhang, 2018). During inference, the matrix $\mathbf{W}^l$ is applied to the output vector from the previous layer $\mathbf{a}^{l-1}$. This is shown in the equation below:

$$\mathbf{z}^l = \mathbf{W}^l \mathbf{a}^{l-1}$$

Here, $\mathbf{a}^0$ corresponds to $\mathbf{x}$. The non-linear function $\sigma : R^d \to R^d$ is then applied to $\mathbf{z}^l$, as shown in equation 2.1. The resulting vector a^l may then again be the input for the following layer.

$$\mathbf{a}^l = \sigma(\mathbf{z}^l) \tag{2.1}$$

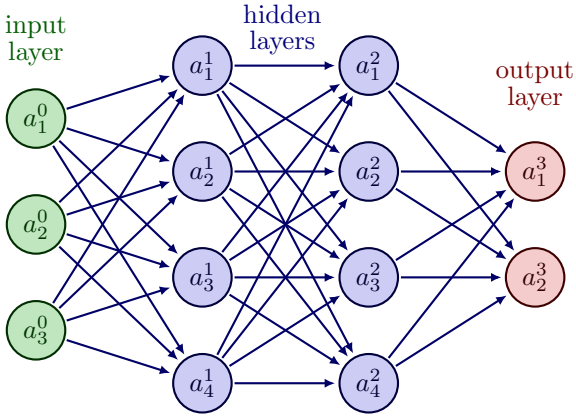

Figure 2.1: Visual representation of a neural network

Hence, during inference, the input vector $\mathbf{x}$ is propagated through each layer, resulting in a final output $\hat{y}^L$. The equation for the forward pass of a neural network with L layers is described as follows:

$$f_{\mathbf{W}^1 \dots \mathbf{W}^L}(x) = \hat{y}^L = \sigma(\dots \sigma(\sigma(x^T \mathbf{W}^1)^T)\mathbf{W}^2 \dots)^T \mathbf{W}^L$$

The architecture of a neural network, which includes the dimensions of the matrices, can be represented as a graph-like figure. An example is shown in 2.1 where the edge-weights between $\mathbf{a}^{l-1}$ and $\mathbf{a}^l$ correspond to the values of in $\mathbf{W}^l$.

However, the parameters $\mathbf{W} = \{\mathbf{W}^1 \dots \mathbf{W}^L\}$ must be learned from a training dataset $\mathcal{D}_{\text{train}} = \{(\mathbf{x}^{(1)}, \mathbf{y}^{(1)}), (\mathbf{x}^{(2)}, \mathbf{y}^{(2)}), \dots\}$. ANNs achieve this through an iterative process of computing how wrong the model is for the training set, and slightly adjusting $\mathbf{W}$ to decrease error rate. This error rate is quantified using a loss function $\mathcal{L}$, which is estimated over a batch of N training samples, shown in the following equation:

$$\mathcal{L}(\mathbf{W}) = \frac{1}{n} \sum_{i=1}^{N} e(\mathbf{y}^{(i)}, \hat{\mathbf{y}}^{(i)})$$

Here, $\mathbf{y}^{(i)}$ corresponds to the ground truth label and $\hat{\mathbf{y}}^{(i)} = f_{\mathbf{W}}(\mathbf{x}^{(i)})$. The error function $e(\cdot)$ can be chosen depending on the task, for instance by mean squared error for regression or cross-entropy for classification problems. The parameters $\mathbf{W}^1 \dots \mathbf{W}^L$ are typically optimised through iterative minimisation of this loss function. This is achieved using backpropagation, an efficient algorithm which computes the partial derivates with respect to each parameter $\mathbf{W}_{ij}^l$. Updating the parameters in the opposite direction of the partial derivative allows for an iterative estimation of a local minimum, which is demonstrated in the following equation using stochastic gradient descent:

$$\mathbf{W}_{ij}^l \leftarrow \mathbf{W}_{ij}^l - \alpha \frac{\partial \mathcal{L}}{\partial \mathbf{W}_{ij}^l}$$

The complexity and power of ANNs are affected by the number of layers and the sizes of the matrices they are composed of. The complexity of the architecture is typically chosen based on the difficulty of the learning problem.

2.1.2 Towards Lower Dimensional Feature Spaces

ANNs' non-linearity combined with the option to define an arbitrary amount of layers, allows the modelling of almost any training set with great accuracies. However, achieving high performance on this training set does not guarantee good generalisation to unseen data (Neyshabur et al., 2017; Chung et al., 2019; Barbiero et al., 2020). As problems become more complex, the use of larger amounts of labelled data is required to ensure good generalisation. Additionally, in the case of a complex feature space $\mathcal{X}$, a more sophisticated architecture may be necessary. However, such complex architectures often require even more data to prevent overfitting and improve generalisation capabilities. The performance of ANNs is thus heavily dependent on the choice of the data representation (Bengio et al., 2013). As a consequence, a lot of effort in the machine learning pipeline is invested in feature engineering (Zheng and Casari, 2018), which involves extracting useful features from the feature space $\mathcal{X}$, removing redundant information, and reducing the dimensionality of the space (Vali et al., 2020) to a lower-dimensional space $\mathcal{Z}$ that is easier to work with. Rather than learning the mapping function directly on the data, $\mathbf{x} \in \mathcal{X}$ is first transformed into a lower-dimensional representation $\mathbf{z} \in \mathcal{Z}$. The mapping function from equation 2.1 is now:

$$f : \mathcal{Z} \to \mathcal{Y}$$

However, feature engineering is a time-consuming and often manual process that requires domain knowledge and expertise (Przybyszewski et al., 2017; Wei et al., 2021). In sections 2.3 and 2.4, we discuss how part of the manual labour of finding good representations from data can be relieved with unsupervised learning approaches, which automate this process. These representations could then be used as the input for a supervised predictor $f(\cdot)$, also known as *downstream task* (Zhang et al., 2021). In the following section, we first provide a brief intermezzo on concepts related to information theory which will prove helpful to understand the underlying principles that these representation learning methods are based on.

2.2 Intermezzo on Information Theory

The formal definitions are obtained from the book "Elements of Information Theory" (Cover and Thomas, 2006). The equations that contain a log function are assumed to be under base two.

2.2.1 Shannon's Entropy

Entropy measures the average amount of information required to describe a random variable (Cover and Thomas, 2006). The entropy $H(X)$ of a discrete random variable X, is formally defined as follows:

$$H(X) = -\sum_{x \in \mathcal{X}} p(x) \log p(x) \tag{2.2}$$

where $\mathcal{X}$ represents the set of events the random variable X can take, formerly known as the *sample space*. Additionally, $p : \mathcal{X} \to [0, 1]$ denotes the probability density function of X. Hence, given an event $x \in \mathcal{X}$, $p(x)$ corresponds to the probability of event x occurring.

Assume a random variable X with possible events x_1, x_2. Intuitively, when $p(x_1)$ is low, the surprise when the event x_1 occurs will be high. The surprise for one event is defined as follows:

$$-\log p(x) \tag{2.3}$$

Hence, entropy can also be considered as the weighted average surprise over each event (Data Science Courses, 2017). To understand why equation 2.3 does indeed correspond to a measure

of surprise, consider an event $x \in \mathcal{X}$ with $p(x) = 1$. Note that $\log p(x) = 0$, and thus the surprise is zero. Meanwhile, if p(x) approaches 0, $\log p(x)$ goes to $-\infty$. And hence, by the negation sign in formula 2.2 the surprise is large.

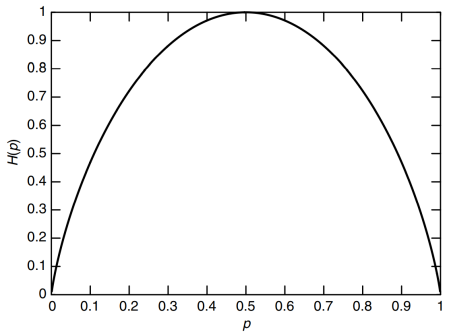

Figure 2.2: $H(p)$ vs p (originates from "Elements of Information Theory", page 16)

Figure 2.2 displays when entropy reaches its maximum for the case of a random variable with 2 outcomes. We can see that the entropy, and thus, the information is largest when the probability of the two outcomes is equal to each other, namely $p(x_1) = p(x_2) = 0.5$. Note that for a random variable X with more than two events, $H(X)$ can be larger than one.

2.2.2 Kullback Leibler Divergence and Mutual Information

The Kullback Leibler (KL) divergence, is defined in equation 2.4, where $p(\cdot)$ and $q(\cdot)$ denote probability density functions over the same sample space $\mathcal{X}$ (Cover and Thomas, 2006). The KL divergence quantifies the "dissimilarity" or "divergence" between the two distributions. Note that $D_{KL}\left(p(\cdot) \mid\mid q(\cdot)\right)$ does not necessarily equal $D_{KL}\left(q(\cdot) \mid\mid p(\cdot)\right)$ and thus the metric is not symmetrical.

$$D_{KL}\left(p(\cdot) \mid\mid q(\cdot)\right) = \sum_{x \in \mathcal{X}} p(x) \log \frac{p(x)}{q(x)} \tag{2.4}$$

The mutual information (MI) between two random variables X and Y can be computed as the KL divergence between their joint probability distribution, $p_{X,Y}(x, y)$, and the product of their marginal probability distributions, $p_X(x)$ and $p_Y(y)$ (Cover and Thomas, 2006). The equation for mutual information then becomes:

$$I(X;Y) = D_{KL}\left(p_{X,Y}(x,y) \mid\mid p_X(x)p_Y(y)\right) \tag{2.5}$$

As described by Cover and Thomas in their book "Elements of Information Theory" (Cover and Thomas, 2006), MI quantifies the amount of information Y describes about X. An alternative definition is illustrated in 2.6. The equation provides us with an intuitive meaning for MI, corresponding to the surprise caused by X, which is reduced by the knowledge of Y.

$$I(X;Y) = H(X) - H(X|Y) \tag{2.6}$$

In sections 2.3 and 2.4, we discuss how these concepts from information theory are applied in representation learning.

2.3 Representation Learning through Reconstruction Error

One of the challenges in supervised learning is the constant need of large amounts of labelled data $\mathcal{D}_{\text{train}} = \{(\mathbf{x}^{(1)}, \mathbf{y}^{(1)}), (\mathbf{x}^{(2)}, \mathbf{y}^{(2)}), \dots\}$. When this set is scarce, or the task becomes too complex to ensure good generalisation, transforming the feature space $\mathcal{X}$ into a lower-dimensional space $\mathcal{Z}$ can be a good solution to aid with learning for the downstream task $f(\cdot)$. Meanwhile, an abundant amount of unlabelled data may already exist. Hence, when a labelled dataset is small, we would like to leverage a larger unlabelled dataset as a basis for learning.

In this section we investigate two self-supervised learning paradigms which learn the following transformation function solely from a feature space $\mathcal{X}$ and thus do not require any labels:

$$T : \mathcal{X} \to \mathcal{Z}$$

The simplified representations obtained from $T(\cdot)$ can then serve as the input for a downstream task as follows:

$$T(\mathbf{x}) = \mathbf{z}$$
$$f(\mathbf{z}) = \mathbf{y}$$

This process of learning a mapping function $T(\cdot)$ which translates a feature vector $\mathbf{x}$ to a lower-dimensional representation $\mathbf{z}$ is commonly referred to as representation learning (Le-Khac et al., 2020).

In the following two subsections, we discuss two paradigms of representation learning with ANNs. The first paradigm learns representations by minimising a reconstruction error. The second learns its representations by contrasting them against noise. These two paradigms will lay the basis for our own contributions in chapter three.

2.3.1 Autoencoders

The encoding problem, introduced by Ackley and Hinton in 1985 (Ackley et al., 1985), and later referred to as the autoencoder by Rumelhart et al. in 1986 (Rumelhart et al., 1988), considers the problem of learning compressed representations through neural networks (Rumelhart et al., 1988; Bank et al., 2021). This is achieved through an ANN architecture consisting of two functions, an *encoder* $E(\mathbf{x}) = \mathbf{z}$ and a *decoder* $D(\mathbf{z}) = \tilde{\mathbf{x}}$. The lower-dimensional *encoding* $\mathbf{z}$ obtained from $E(\mathbf{x})$ will then serve as representation for downstream task $f(\cdot)$. The functions $E(\cdot)$ and $D(\cdot)$ are simultaneously optimised by minimising the reconstruction error shown in the following equation:

$$\mathcal{L} = \sum_{i=1}^{N} l(\mathbf{x}^{(i)}, \tilde{\mathbf{x}}^{(i)}) \tag{2.7}$$

where l refers to the error for a single data point, for instance, the L^2-norm, and N the number data points. The dimension of $\mathbf{z}$ is typically smaller than the original dimension of $\mathbf{x}$. This results in the encoder having to define encodings that are as "informative" as possible to reconstruct the original data (Bank et al., 2021).

An example autoencoder architecture is depicted in figure 2.3. Since an autoencoder is in fact a single ANN and $\mathbf{z}$ corresponds to the output produced by an intermediate hidden layer, $\mathbf{z}$ is also commonly referred to as a *latent* representation. The space of all latent representations $\mathcal{Z}$ is known as the *latent* space. While capable of learning compressed representations, autoencoders do not pose any restrictions on the latent space $\mathcal{Z}$. As a result, the representations may be

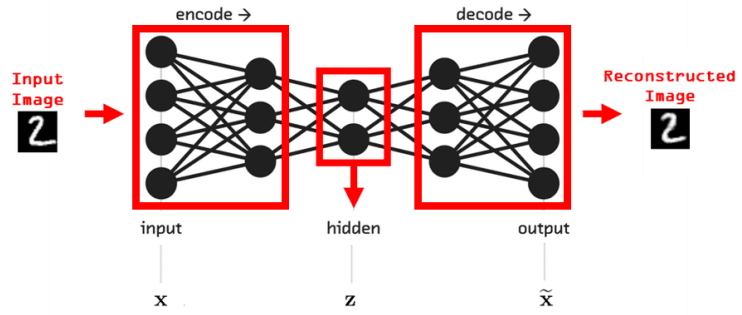

Figure 2.3: Autoencoder architecture, adapted from (Karagiannakos, 2018).

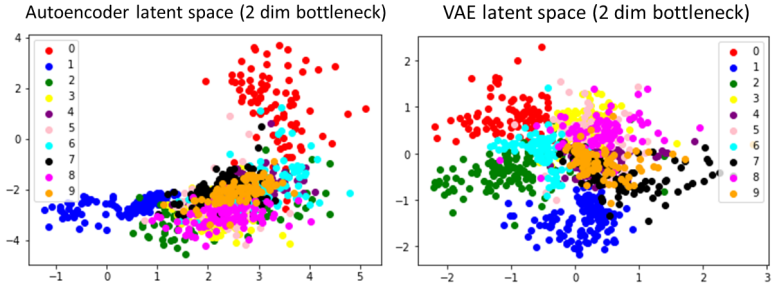

Figure 2.4: Latent space of autoencoder (left) and VAE (right), learned from the MNIST dataset, a dataset consisting of images of handwritten digits between 0 and 9 (Lecun et al., 1998). The ANNs have not received any explicit information of the labels of the dataset.

meaningful to computers, but non-interpretable to humans. For instance, given the left image depicted in figure 2.4 which depicts an autoencoder's two-dimensional latent space, it is almost impossible to infer in advance what the corresponding digit would be when interpolating a new $\mathbf{z}$ somewhere in between the encodings corresponding to digit 0 (red) and 1 (blue). In addition, slight changes to $\mathbf{z}$ may result in significant changes to its decoded counterpart $\mathbf{x}$. Finally, attempting to understand an autoencoder's latent space $\mathcal{Z}$ becomes even more infeasible as the dimension of $\mathcal{Z}$ increases.

2.3.2 Variational autoencoders

Similar to traditional autoencoders, variational autoencoders (VAE) learn representations that contain the important information necessary to reconstruct the data. VAEs maintain the same structure as autoencoders, consisting of an encoder $E(\mathbf{x}) = \mathbf{z}$ and decoder $D(\mathbf{z}) = \tilde{\mathbf{x}}$. However, an additional constraint is applied to the latent space $\mathcal{Z}$ (Doersch, 2021; David Foster, 2023; Kingma and Welling, 2022, 2019; Cinelli et al., 2021). The latent representations $E(\mathbf{x}) = \mathbf{z}$ are samples from multivariate distributions, which we will denote by

$$\mathbf{z} \sim q(\mathbf{z} \mid \mathbf{x}) \quad \text{which is also written as:} \quad \mathbf{z} \sim q(\cdot \mid \mathbf{x})$$

Thus, given a feature vector $\mathbf{x}$, we obtain its corresponding *encoding* or *latent representation* $\mathbf{z}$ by taking a sample from a distribution. This distribution is commonly known as the *posterior* distribution, we will define it in more detail in a following paragraph. The encoder function $E(\cdot)$

in VAEs is thus nondeterministic and computing $E(\mathbf{x}) = \mathbf{z}$ twice may result in two different $\mathbf{z}$s both corresponding to the same $\mathbf{x}$. In a following paragraph, we will discuss how to achieve this nondeterministic behaviour using ANNs.

By defining the latent representations as samples from distributions, we can pose the same constraints on the quality of the representations $\mathbf{z} \in \mathcal{Z}$ as in traditional autoencoders, but also additional constraints on how the latent space $\mathcal{Z}$ is organised. The additional constraints posed by VAEs on $\mathcal{Z}$ will result in a more interpretable space, where $\mathbf{z}$'s underlying components can be better understood. This will be achieved by enforcing each distribution $q(\cdot \mid \mathbf{x}^{(i)})$ corresponding to a particular $\mathbf{x}^{(i)}$, to be "similar" to a chosen *prior* distribution $p(\mathbf{z})$. Typically, the prior $p(\mathbf{z})$ is set to the standard normal distribution $\mathcal{N}(\mathbf{0}, \mathbf{I})$ (David Foster, 2023). The result of this setup can be observed in the latent space depicted in the right plot of figure 2.4 where all $\mathbf{z}$s are attracted to the origin.

In the following subsections, we will explore VAEs in more detail. We begin with a discussion on the process of imposing constraints on $\mathcal{Z}$, which leads to the VAE loss function. Next, we investigate how ANNs can be utilised to simulate sampling from distributions. Finally, we examine how VAEs enable the creation of interpretable representations and how they can be used to generate novel data.

The loss function

So far, we have learned that Variational Autoencoders (VAEs) use an encoder $E(\mathbf{x}) = \mathbf{z}$ to create a latent representation $\mathbf{z}$ of the input feature vector $\mathbf{x}$, where $\mathbf{z}$ is a sample from the distribution $\mathbf{z} \sim q(\mathbf{z} \mid \mathbf{x})$. We can then define $q(\mathbf{z} \mid \mathbf{x})$ as a Gaussian with independent components, parametrised by $\boldsymbol{\mu}$ and covariance matrix $\text{diag}(\boldsymbol{\sigma})$. We obtain the following definition:

$$q(\mathbf{z} \mid \mathbf{x}) = \mathcal{N}(\boldsymbol{\mu}, \text{diag}(\boldsymbol{\sigma})) \tag{2.8}$$

where $\text{diag}(\boldsymbol{\sigma})$ denotes the covariance matrix with $\boldsymbol{\sigma}$ on the diagonal and zeroes elsewhere. It is important to recognise that $\boldsymbol{\mu}$ and $\boldsymbol{\sigma}$ are different for every $\mathbf{x}$. The two parameters will be computed by an ANN.

The representations are optimised to minimise two measurements: one, the reconstruction error, and secondly, the dissimilarity from the latent distributions to a chosen prior $p(\mathbf{z})$. The loss function to be optimised for a single data point $\mathbf{x}^{(i)}$ is shown in the equation below.

$$\mathcal{L}(\mathbf{x}^{(i)}) = \mathop{\mathbb{E}}_{\mathbf{z}^{(i)} \sim q(\cdot \mid \mathbf{x}^{(i)})} \Big[-\log p(\mathbf{x}^{(i)} \mid \mathbf{z}^{(i)}) \Big] + D_{KL} \Big(q(\cdot \mid \mathbf{x}^{(i)}) \mid\mid p(\cdot) \Big) \tag{2.9}$$

Here, $p(\cdot)$ refers to the prior distribution, which is different from $p(\mathbf{x}^{(i)} \mid \mathbf{z}^{(i)})$. Although $\mathcal{L}$ may seem daunting at first, we will decompose its components. The loss function is made up of two terms, the left term corresponds to the reconstruction error, while the second term poses constraints on the latent space. Let us focus on the reconstruction term first.

$$\mathop{\mathbb{E}}_{\mathbf{z}^{(i)} \sim q(\cdot \mid \mathbf{x}^{(i)})} \Big[-\log p(\mathbf{x}^{(i)} \mid \mathbf{z}^{(i)}) \Big] \tag{2.10}$$

In a traditional autoencoder we optimise $D(E(\mathbf{x}^{(i)})) = \tilde{\mathbf{x}}^{(i)}$ such that $\mathbf{x}^{(i)} \approx \tilde{\mathbf{x}}^{(i)}$. We will now show that the reconstruction term in equation 2.10 achieves a similar goal for VAEs. Here, $p(\mathbf{x}^{(i)} \mid \mathbf{z}^{(i)})$ is a distribution over $\mathbf{z}^{(i)}$ where $\mathbf{x}^{(i)}$ is fixed, and the latent representation $\mathbf{z}^{(i)} = E(\mathbf{x}^{(i)})$ is sampled from the Gaussian distribution $\mathbf{z}^{(i)} \sim q(\cdot \mid \mathbf{x}^{(i)})$. The objective is to ensure that $D(\mathbf{z}^{(i)}) \approx \mathbf{x}^{(i)}$. However, since $\mathbf{z}^{(i)}$ is sampled from a Gaussian distribution, the $\mathbf{z}^{(i)}$'s close to the mean $\boldsymbol{\mu}^{(i)}$ are more likely to be sampled than those further away. Thus, for these $\mathbf{z}^{(i)}$'s,

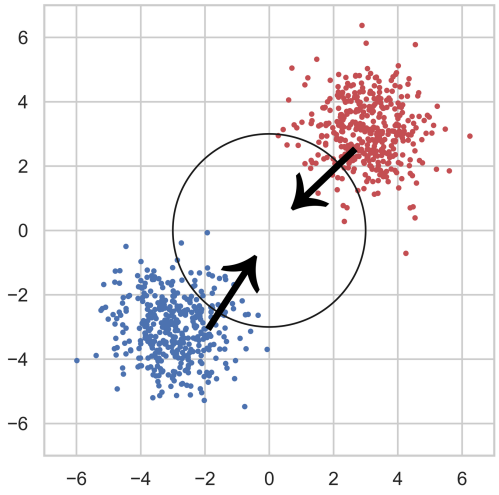

Figure 2.5: 200 samples $\mathbf{z}^{(i)}$ and $\mathbf{z}^{(j)}$ from feature vectors $\mathbf{x}^{(i)}$ and $\mathbf{x}^{(j)}$, respectively, represented by red and blue data points. The prior $p(\mathbf{z})$ is set to the standard normal, and the regularisation term of VAE's loss pushes the latent space towards the origin.

we'd like the probability of corresponding to the actual $\mathbf{x}^{(i)}$ to be high, or equivalently we want $p(\mathbf{x}^{(i)} \mid \mathbf{z}^{(i)}) \approx 1$ (Cinelli et al., 2021). Finally, by adding a negative sign in front, maximising this probability is equivalent to minimising the negative probability. In practice, this term is approximated through mini-batches with the mean squared error.

Optimising the second term of equation 2.9 poses the constraints on the distributions $q(\cdot \mid \mathbf{x}^{(i)})$.

$$D_{KL}\left(q(\cdot \mid \mathbf{x}^{(i)}) \,||\, p(\cdot)\right) \tag{2.11}$$

Again, this metric should be minimised. As we discussed in chapter 2.2.2, KL divergence can be considered as a dissimilarity measure between two distributions. Hence, this value is small when the two distributions are similar. The prior distribution $p(\cdot)$ is a fixed distribution which is chosen by the user, typically defined as $\mathcal{N}(\mathbf{0}, \mathbf{I})$. Minimising this metric will result in moving each distribution $q(\mathbf{z} \mid \mathbf{x}^{(i)})$, corresponding to a value $\mathbf{x}^{(i)}$, close to $\mathcal{N}(\mathbf{0}, \mathbf{I})$. This idea is depicted in figure 2.5. When $p(\cdot) = \mathcal{N}(\mathbf{0}, \mathbf{I})$, equation 2.11 becomes:

$$D_{KL}\left(q(\cdot \mid \mathbf{x}^{(i)}) \,||\, \mathcal{N}(\mathbf{0}, \mathbf{I})\right)$$

When $q(\cdot \mid \mathbf{x}^{(i)}) = \mathcal{N}(\boldsymbol{\mu}^{(i)}, \text{diag}(\boldsymbol{\sigma}^{(i)}))$, one can algebraically prove, that optimising the above equation is equivalent to optimising the following (Kingma and Welling, 2022):

$$D_{KL}\left(\mathcal{N}(\boldsymbol{\mu}^{(i)}, \text{diag}(\boldsymbol{\sigma}^{(i)})) \,||\, \mathcal{N}(\mathbf{0}, \mathbf{I})\right) = \frac{1}{2}\sum_{k=1}^{D}\left(-\log(\sigma_k^{(i)})^2 - 1 + (\sigma_k^{(i)})^2 + (\mu_k^{(i)})^2\right) \tag{2.12}$$

where $\sigma_k^{(i)}$ and $\mu_k^{(i)}$ correspond to the components of the predicted vectors $\boldsymbol{\sigma}^{(i)}$ and $\boldsymbol{\mu}^{(i)}$, respectively. The latent space has dimensionality D.

Simulating distributions through neural networks

Computing $E(\mathbf{x}^{(i)})$ results in an encoding $\mathbf{z}^{(i)}$ which is sampled from $\mathbf{z}^{(i)} \sim q(\cdot \mid \mathbf{x}^{(i)})$. We will now discuss how ANNs can emulate the stochastic behaviour of sampling from a distribution. As discussed in equation 2.8, distribution $q(\cdot \mid \mathbf{x}^{(i)})$ is parametrised as a factorised Gaussian with mean $\boldsymbol{\mu}^{(i)}$ and covariance matrix $\text{diag}(\boldsymbol{\sigma}^{(i)})$. The entire distribution can thus be modelled by an ANN which takes as input $\mathbf{x}^{(i)}$ and generates the two corresponding vectors $\boldsymbol{\mu}^{(i)}$ and $\boldsymbol{\sigma}^{(i)}$. Finally, a sample $\mathbf{z}^{(i)}$ can be obtained as follows:

$$\mathbf{z}^{(i)} = \boldsymbol{\mu}^{(i)} + \boldsymbol{\sigma}^{(i)} \odot \boldsymbol{\epsilon}^{(i)} \tag{2.13}$$

where $\boldsymbol{\epsilon}^{(i)}$ corresponds to a sampled value $\boldsymbol{\epsilon}^{(i)} \sim \mathcal{N}(\mathbf{0}, \mathbf{I})$ and $\odot$ is element-wise multiplication. Computing $\mathbf{z}^{(i)}$ through $\boldsymbol{\epsilon}^{(i)}$, rather than directly sampling from $\mathbf{z}^{(i)} \sim \mathcal{N}(\boldsymbol{\mu}^{(i)}, \text{diag}(\boldsymbol{\sigma}^{(i)}))$ is referred to as the parametrisation trick and allows for gradients to freely backpropagate through the layer (David Foster, 2023). The decoder $D(\mathbf{z}^{(i)}) = \tilde{\mathbf{x}}^{(i)}$ can remain identical to the traditional autoencoder's decoder. An overview is presented in figure 2.6.

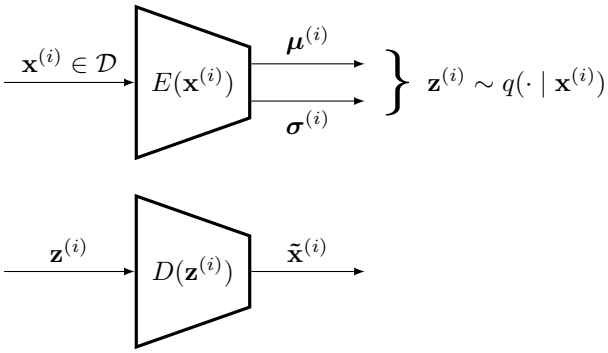

Figure 2.6: High level view of a VAE.

Generating new data and interpretability

Due to the VAE's regularisation term, all encodings are pushed towards the centre as depicted in figure 2.5. Additionally, the space of encodings corresponding to a single $\mathbf{x}^{(i)}$ is an entire neighbourhood around a particular $\boldsymbol{\mu}$ and $\boldsymbol{\sigma}$. These two properties ensure a well-covered and uninterrupted space around the origin with smooth transitions on the generative factors between latent representations (David Foster, 2023). As a result, new samples from the dataset can be generated by discarding the VAE's encoder and providing standard normal noise to the decoder instead. It is important to understand that this method only works for VAEs and not for the traditional autoencoder. This is because autoencoders do not pose any additional constraints on the latent space. Generating new data points from random noise via a traditional autoencoder may result in nonsense generations as the random noise may be too different from the latent space it was trained on. As a result, there are no guarantees that the autoencoder's decoder will generalise to these random representations.

Additionally, for the same reason, we can interpolate between encodings obtained from the data. The interpolated encoding can then decoded to the original space. We can observe the specific information contained in each of the representations' features through the decoder, resulting in a significant improvement in interpretability.

Disentanglement of latent representations and posterior collapse

Higgins et al. (2022) extend the VAE framework through the introduction of a slight modification of the loss function, resulting in β-VAE. An additional hyper-parameter β is introduced to the VAE's loss function which controls the weight of the regularisation term:

$$\mathcal{L}_{\theta,\phi}(\mathbf{x}^{(i)}) = \mathop{\mathbb{E}}_{\mathbf{z}^{(i)}\sim q(\cdot|\mathbf{x}^{(i)})} \Big[-\log p(\mathbf{x}^{(i)} \mid \mathbf{z}^{(i)}) \Big] + \beta \; D_{KL} \Big(q(\cdot \mid \mathbf{x}^{(i)}) \;||\; p(\cdot) \Big)$$

Setting the prior to a standard normal distribution ($p(\mathbf{z}) = \mathcal{N}(\mathbf{0}, \mathbf{I})$) encourages disentangled representations, where each variable is sensitive to a specific generative factor (Higgins et al., 2022; Bengio et al., 2013). For example, in an image of a face, altering one component of the representation would only change the smile, while other features like skin colour and brightness remain constant. Such disentangled representations are interpretable, making it easier to understand the underlying structure of the representation and what information each variable contains.

However, a trade-off must be made between accuracy and disentanglement. A small β value (close to 0) results in high a reconstruction accuracy but weak constraints on disentanglement, while a large β value (above 1) puts large emphasises on disentanglement at the cost of accuracy. If β becomes too large, the posteriors $q(\mathbf{z} \mid \mathbf{x}^{(i)})$ corresponding to each data point $\mathbf{x}^{(i)}$ can become equal to the prior $p(\mathbf{z})$, resulting in no information contribution, which is known as posterior collapse (Lucas et al., 2022).

2.4 Representation learning through Noise Contrastive Estimation

In the following two sections, we discuss Contrastive Predictive Coding (CPC) and Greedy InfoMax (GIM). We will use GIM as the basis for our own experiment in the following chapter. However, GIM continues from the concepts introduced in CPC and a good understanding is needed to understand the contributions of GIM.

2.4.1 Contrastive Predictive Coding

CPC is an unsupervised learning approach, again with the objective of learning (lower-dimensional) representations from high dimensional data (van den Oord et al., 2019). While the objective is thus the same as for the autoencoders discussed in the previous section, CPC achieves its representations entirely differently. An autoencoder's objective is to define a compressed representation from which the original data can be recovered. However, when working with sequential data $\mathbf{x}_1, \mathbf{x}_2, \ \ldots, \ \mathbf{x}_t, \ \ldots$, simply compressing patches $\mathbf{x}_i$ of the sequence without considering the relation with nearby patches can result in suboptimal encodings, as contextual information between patches is not encoded directly into the representation (Shah, 2020).

CPC deals with these context issues by maximising the shared information between the extracted representations of temporally nearby patches (Löwe et al., 2020). We will discuss this concept in more detail in this section. For now, we would like to draw the reader's attention to figure 2.7. The figure depicts a high-level view of how this idea is achieved by producing two latent representations $\mathbf{z}_i$ and $\mathbf{c}_i$. An audio sequence of undefined length is split up into patches $\mathbf{x}_1 \ldots \mathbf{x}_n$ where each $\mathbf{x}_i$ is a vector of fixed length, containing for instance 10ms of speech audio. Each patch $\mathbf{x}_i$ is encoded into latent representation $\mathbf{z}_t$, defined as follows:

$$\mathbf{z}_t = g_{enc}(\mathbf{x}_t).$$

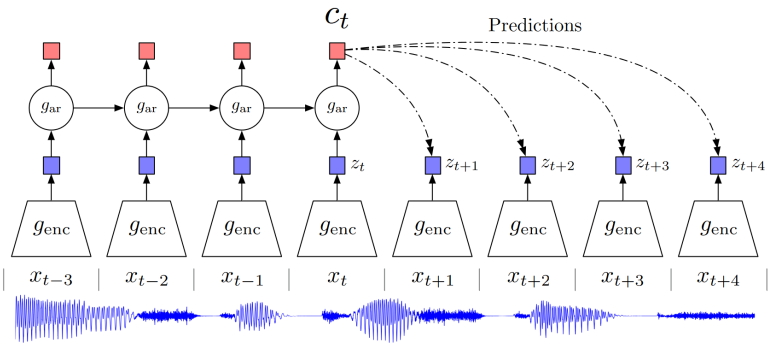

Figure 2.7: Overview of Contrastive Predictive Coding, originates from (van den Oord et al., 2019).

$g_{enc}(\cdot)$ is for instance a ConvNet. The latent representations $\mathbf{z}_1 \dots \mathbf{z}_n$ are obtained independently from each other and do not yet contain any contextual information. This is achieved through $g_{ar}(\cdot)$, an autoregressor, which encodes all previous $\mathbf{z}_1 \dots \mathbf{z}_t$ into a single representation $\mathbf{c}_t$:

$$\mathbf{c}_t = g_{ar}(\mathbf{z}_1 \dots \mathbf{z}_t)$$

Either $\mathbf{z}_t$ or $\mathbf{c}_t$ could be used as the latent representation for downstream tasks. van den Oord et al. (2019) suggest using $\mathbf{c}_t$ for tasks where context about the past is useful, for instance, speech recognition, and $\mathbf{z}_t$ when the historic context is not useful. As shown in figure 2.7, the encodings from sequential data of undefined length, may correspond to a series of latent representations $\mathbf{c}_1, \mathbf{c}_2, \dots$ or $\mathbf{z}_1, \mathbf{z}_2, \dots$. In the case of downstream tasks which require a single representation vector, van den Oord et al. propose to pool the sequence of vector representations into a single vector.

Slowly varying features

The temporally nearby patches $\mathbf{z}_{t+1}$ and $\mathbf{c}_t$ are optimised to preserve shared information, while discarding differences. Before we discuss how to obtain such representations, we first motivate why defining representations in this fashion makes sense.

Consider we would like to define useful representations for sequential data such as speech signals. Then it is not unlikely to believe that the conveyed information at time step t and $t + k$ contains some redundancy, such as pitch, frequency, tone, etc. (Rao, 2020). Meanwhile, large changes of the signal in a small time window may be the result of noise. Sequential data which poses these slowly varying features are commonly referred to as "slow-features" (Zhang and Tao, 2012). CPC leverages these slowly varying features, by encoding the underlying shared information between different patches while at the same time discarding low-level information and noise that is more local (van den Oord et al., 2019).

The loss function

CPC learns preserve information between temporally nearby representations, by solving another task. In particular, CPC learns to discriminate subsequent *positive* samples $\mathbf{z}_{t+k}$ from *negative* random samples $\mathbf{z}_j$. This is achieved through a similarity function $f_k(\cdot)$, which scores the similarity between two latent representations (Löwe et al., 2020). It is defined as a log bilinear model

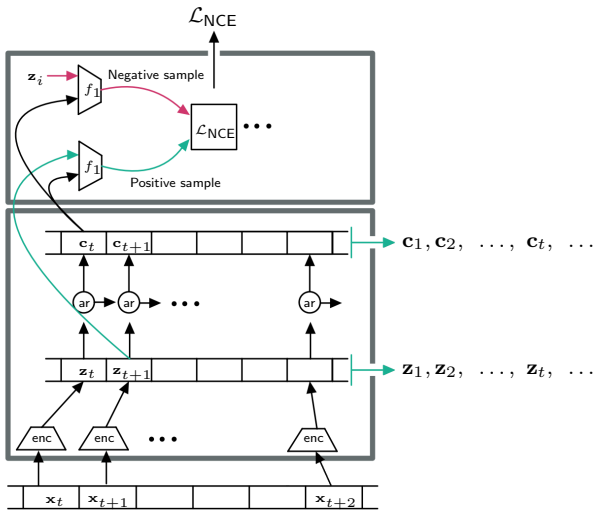

Figure 2.8: Overview of CPC. The encoder, autoregressor and $f_k(\cdot)$ are ANNs and their parameters are optimised via $\mathcal{L}_{\text{NCE}}$.

as follows:

$$f_k(\mathbf{z}_j, \mathbf{c}_t) = \exp(\mathbf{z}_j^T W_k \mathbf{c}_t) \tag{2.14}$$

where W_k is a weight matrix which is learned. $f_k(\mathbf{z}_j, \mathbf{c}_t)$ thus quantifies how likely the context $\mathbf{c}_t$ corresponds to a random vector $\mathbf{z}_j$. Due to the slowly varying data assumption, a good representation for successive representations $\mathbf{z}_{t+k}$ and $\mathbf{c}_t$ is one where $f_k(\mathbf{z}_{t+1}, \mathbf{c}_t)$ is high and $f_k(\mathbf{z}_j, \mathbf{c}_t)$ is small for random $\mathbf{z}_j$. Or equivalently, maximising the shared information between temporally nearby patches, while discarding the temporal noise results in large values $f_k(\mathbf{z}_{t+1}, \mathbf{c}_{t+1})$.

The InfoNCE loss, used to optimise g_{enc}, g_{ar} and W_k simultaneously is shown below.

$$\mathcal{L}_{\text{NCE}} = -\sum_k \mathop{\mathbb{E}}_{\text{X}} \left[\log \frac{f_k(\mathbf{z}_{t+k}, \mathbf{c}_t)}{\sum_{\mathbf{z}_j \in X} f_k(\mathbf{z}_j, \mathbf{c}_t)} \right] \tag{2.15}$$

Here, X corresponds to the set $\{\mathbf{z}_{t+k}, \mathbf{z}_1, \mathbf{z}_2, \ldots\}$. Notice that there exists exactly one $\mathbf{z}_{t+k} \in X$, which corresponds to a positive sample for $\mathbf{c}_t$ and all other $\mathbf{z}_j \in X$ are negative samples. Hence good representations should result in a large similarity score $f_k(\mathbf{z}_{t+k}, \mathbf{c}_t)$, while $f_k(\mathbf{z}_i, \mathbf{c}_t) \approx 0$ for negative samples, resulting in a fraction equal to 1. This would lead to a loss of 0 by the $\log(\cdot)$ function. On the other hand, $\mathcal{L}_{\text{NCE}}$ is large when the denominator is large, which occurs when $f(\cdot)$ is often unsure about negative samples and produces large values for those as well. An overview of the three ANNs which each must be optimised is depicted in figure 2.8.

Ties with mutual information

Earlier we argued that CPC's latent representations will preserve shared information between temporally nearby patches, while discarding the local noise. van den Oord et al. (2019) make this claim even stronger by making ties with mutual information, which we discussed in a previous chapter. In particular, van den Oord et al. prove that optimising InfoNCE is equivalent to maximising the mutual information between $\mathbf{c}_t$ and $\mathbf{z}_{t+1}$:

$$I(\mathbf{z}_{t+1}; \mathbf{c}_t) = \sum_{\mathbf{z}_{t+1}, \mathbf{c}_t} p(\mathbf{z}_{t+1}, \mathbf{c}_t) \log \frac{p(\mathbf{z}_{t+1} \mid \mathbf{c}_{t+1})}{p(\mathbf{z}_{t+1})} \tag{2.16}$$

This proof is available in their appendix. Although we do not repeat the proof here, we give a high-level overview.

The first step in proving the relationship between the InfoNCE loss and mutual information is to model $f_k(\mathbf{z}_{t+k}, \mathbf{c}_t)$ in a probabilistic manner. The InfoNCE loss is in fact the categorical cross-entropy of classifying the positive sample correctly with $\frac{f_k}{\sum_X f_k}$ as the predicted model (van den Oord et al., 2019). Since this equation may take values between zero and one, it can be considered as a probability. In particular, the optimal probability for the loss can then be written as

$$p(i \mid X, \mathbf{c}_t)$$

where X corresponds the set of samples $\{\mathbf{z}_{t+k}, \mathbf{z}_1, \mathbf{z}_2, \dots\}$ as discussed in the InfoNCE loss, and i corresponds to indicator that sample $\mathbf{z}_i$ is the "positive" sample. By doing so, one can eventually obtain a proportionality relation to the density distribution presented below.

$$f_k(\mathbf{z}_{t+k}, \mathbf{c}_t) \propto \frac{p(\mathbf{z}_{t+k} \mid \mathbf{c}_t)}{p(\mathbf{z}_{t+k})} \tag{2.17}$$

van den Oord et al. (2019) utilise this proportionality relation to reformulate $-\mathcal{L}_{\text{NCE}}$ as a lower bound on the mutual information between $\mathbf{z}_{t+1}$ and $\mathbf{c}_t$ as follows:

$$I(\mathbf{z}_{t+1}; \mathbf{c}_t) \geq \log(N) - \mathcal{L}_{\text{NCE}} \tag{2.18}$$

Since the number of samples N is a constant, the mutual information between $\mathbf{z}_{t+1}$ and $\mathbf{c}_t$ becomes greater when $\mathcal{L}_{\text{NCE}}$ becomes smaller. Additionally, when the number of samples N increases, the bound becomes tighter.

2.4.2 Greedy InfoMax

So far we discussed how CPC encodes patches of sequential data into latent representations by maximising the mutual information between temporally nearby representations. This method has shown great success in recent years and is considered state-of-the-art in self-supervised learning for encoding sequential data (Stacke et al., 2020). Additionally, CPC has been successfully applied to multiple use cases (Stacke et al., 2020; de Haan and Löwe, 2021; Lu et al., 2019; Bhati et al., 2021; Deldari et al., 2021; Henaff, 2020). This is achieved by minimising the InfoNCE loss discussed earlier in equation 2.15. Through this *global* loss function all parameters are optimised end-to-end via backpropagation.

Even though empirical evidence has shown that backpropagation is highly effective (Krizhevsky et al., 2012; Ioffe and Szegedy, 2015), it still suffers from multiple constraints. Firstly, there is a biological perspective to consider, as the human brain lacks a global objective function that can be optimised by backpropagating an error signal (Marblestone et al., 2016). This is especially significant when considering how children can learn to categorise from a few examples, whereas end-to-end backpropagation often requires extensive datasets to achieve good generalisation (Löwe et al., 2020). Moreover, end-to-end backpropagation also suffers from computational constraints, such as requiring the entire computational graph, including all parameters, activations and gradients to fit in memory (Löwe et al., 2020). Additionally, during the training process of a neural network, each layer has to wait for the gradients of its subsequent layer, which reduces locality and impedes the efficiency of hardware accelerator design (Löwe et al., 2020).

Towards greedy learning

To overcome these computational constraints, Löwe et al. (2020) introduce Greedy InfoMax (GIM), an extension on CPC inspired by the biological brain. Whereas CPC obtains representations $\mathbf{z}_t$ and $\mathbf{c}_t$ through encoder $g_{enc}(\cdot)$ and autoregressor $g_{ar}(\cdot)$, GIM splits $g_{enc}(\cdot)$'s neural network architecture by depth into M so-called "*modules*":

$$g^1_{enc}(\cdot),\ g^2_{enc}(\cdot),\ \ldots,\ g^M_{enc}(\cdot)$$

A single module may for instance represent one or more layers. Each module's output is the input of the successive module.

$$g^m_{enc}(\mathbf{z}^{m-1}_t) = \mathbf{z}^m_t$$
$$g_{ar}(\mathbf{z}^M_1\ \ldots\ \mathbf{z}^M_t) = \mathbf{c}_t$$

The final representation $\mathbf{z}^M_t$ is obtained by propagating $\mathbf{x}_t$ through each module as follows:

$$g^M_{enc}(\ldots g^2_{enc}(g^1_{enc}(\mathbf{x}_t))) = \mathbf{z}^M_t$$

Both $\mathbf{z}^M_t$ or $\mathbf{c}_t$ may serve as the representation for downstream tasks.

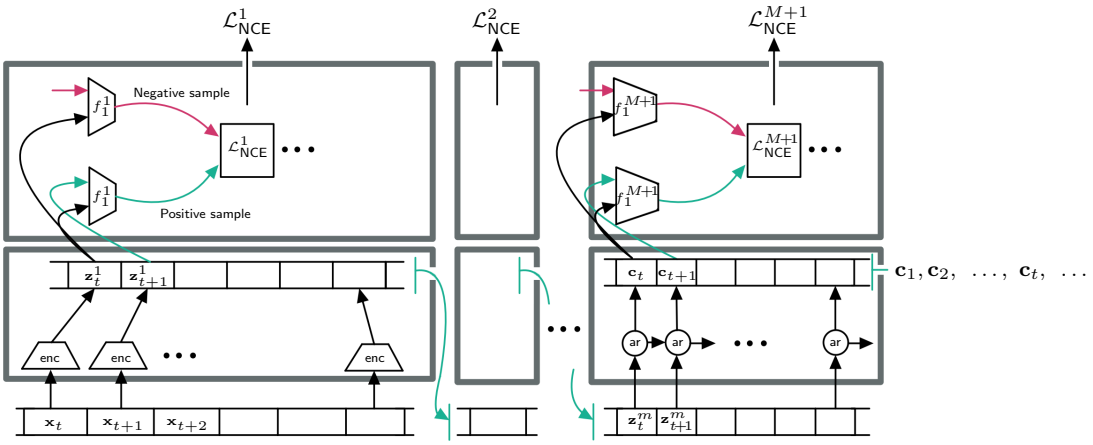

Figure 2.9: Overview of Greedy InfoMax

Each module $g^m_{enc}(\cdot)$ is *greedily* optimised with an adaptation of the InfoNCE loss, introduced in CPC. This idea is depicted in figure 2.9, which displays M modules, each trained with their own instance of the InfoNCE loss.

In contrast to CPC where a single loss function $\mathcal{L}_{\text{NCE}}$ and scoring function $f_k(\cdot)$ are required, we now require $\mathcal{L}^m_{\text{NCE}}$ and $f^m_k(\cdot)$ for each module. The equations to optimise for $g^m_{enc}(\cdot)$ then become:

$$f^m_k(\mathbf{z}^m_{t+k}, \mathbf{z}^m_t) = \exp({\mathbf{z}^m_{t+k}}^T W^m_k \mathbf{z}^m_t) \tag{2.19}$$

$$\mathcal{L}^m_{\text{NCE}} = -\sum_k \mathop{\mathbb{E}}_{X} \left[\log \frac{f^m_k(\mathbf{z}^m_{t+k}, \mathbf{z}^m_t)}{\sum_{\mathbf{z}^m_j \in X} f^m_k(\mathbf{z}^m_j, \mathbf{z}^m_t)} \right] \tag{2.20}$$

From equation 2.19, we observe that $f^m_k(\cdot)$ no longer receives as input an aggregate $\mathbf{c}_t$, but instead a second $\mathbf{z}_t$. This is in contrast to CPC where $f^m_k(\mathbf{z}^m_{t+k}, \mathbf{c}^m_t)$ is maximised instead.

GIM thus omits the autoregressive function within each module. Optionally, for downstream tasks where broad context is helpful, such as the classification of phonetic structures in speech recognition, an autoregressive model $g_{ar}(\mathbf{z}_1^M \ \dots \ \mathbf{z}_t^M) = \mathbf{c}_t$ can be appended as a final $M+1$'th module. The altered scoring function then becomes:

$$f_k^{M+1}\left(\mathbf{z}_{t+k}^M, \mathbf{c}_t\right) = \exp\left({\mathbf{z}_{t+k}^M}^T W_k^{M+1} c_t\right)$$

As a result of this approach, the mutual information $I(\mathbf{z}_{t+k}^m, \mathbf{z}_t^m)$ is maximised, rather than $I(\mathbf{z}_{t+k}, \mathbf{c}_t)$ as in CPC.

As a result of GIM's greedy approach, modules can be trained in parallel, but also sequentially. By training one module after the other, the memory cost can be decreased during training which is beneficial for memory-constrained scenarios. Furthermore, when a higher level of abstraction is needed, additional modules can be appended to the architecture later on without having to fine-tune previous modules. In the following chapter, we discuss how we can maintain these benefits in V-GIM, while also allowing for better interpretability.

Chapter 3

Variational Greedy InfoMax

3.1 Motivations

In the previous chapter, we discussed two frameworks of deep representation learning. First, we discussed the autoencoder and its variational counterpart, which minimise the reconstruction error. Secondly, we discussed Contrastive Predictive Coding (CPC) and Greedy InfoMax (GIM), both of which optimise the InfoNCE objective. These two approaches seek to maximise the mutual information between the encodings of data patches that are temporally nearby. The latent representations obtained from all four methods can then be utilised for downstream tasks (Bengio et al., 2013; Wei and Mahmood, 2021; van den Oord et al., 2019; Löwe et al., 2020)

The autoencoder's sole objective is to learn lower dimensional representations of which the original data can be reconstructed. As a result, the representations may serve well for data compression, but no additional constraints are enforced, such as feature disentanglement and thus the latent space may still be hard to work with for downstream tasks (Tschannen et al., 2018). Meanwhile, VAEs with a standard normal prior, enforce representations which break down or disentangle each feature into a narrowly defined variable and encode them as separate dimensions (Wei and Mahmood, 2021). This additional constraint could potentially result in better-suited representations for downstream tasks. To understand why, consider for instance a classifier which is tasked to predict the pronounced syllables corresponding to the latent representation of a speech wave. It would then be beneficial to have all syllable-related information encoded in specific dimensions, which are not influenced by other audio properties, such as the speaker's identity.

Both autoencoders and VAEs assess the quality of their representations by comparing the original data with its reconstruction. Consequently, their architectures require an additional decoder block, which must also fit into memory. This can be a disadvantage for resource-constrained devices, as the overhead from the decoder restricts the architectures that these devices can train. Meanwhile, CPC and V-GIM learn representations without having to reconstruct the original data. As a result, they do not require a decoder and can benefit from a simplified architecture, while, maintaining state-of-the-art performance (Stacke et al., 2020). A second benefit of CPC and GIM is that they are directly compatible with sequential data.

Both frameworks (reconstruction and information maximisation algorithms) possess the ability to obtain useful representations for various downstream tasks. However, the content of these representations may not always be intuitive to humans and their structure may be difficult to comprehend. While CPC and GIM are considered state-of-the-art, their performance comes at a cost of having the least interpretable representations. Autoencoders maintain interpretability

because a decoder can be used to reveal the information contained in the latent representation. The same transparency can also be achieved with VAEs. Additionally, by using a standard Gaussian as a prior and constraining the latent distributions to be similar to this prior, we can interpolate between representations and observe the effects through the decoder. As such, we can observe the specific information that is contained in each of the representation's components (channels in ConvNets or neurons in fully connected ANNs). VAEs can also result in disentangled features, further enhancing interpretability (Grossutti et al., 2022). In contrast, CPC and GIM do not contain a built-in decoder mechanism, nor pose constraints on the latent space, significantly reducing interpretability.

3.2 Towards Decoupled Training for Probabilistic Representations

In what follows next we introduce Variational Greedy InfoMax (V-GIM), maintaining the state-of-the-art performance obtained from optimising the InfoNCE objective, while leveraging the interpretable and disentangled benefits from VAEs. This is achieved by optimising a novel loss function, *Variational-InfoNCE*, a combination of InfoNCE and the regularisation term from VAEs. Additionally, by splitting up the neural network into modules, as introduced in (Löwe et al., 2020), we greedily optimise each module with its own instance of this loss function. As a result, the interpretability benefits from VAEs will also be applicable in-between modules. This is in contrast to VAEs where solely the final output representations are interpretable.

As discussed in the section on CPC, a patch of sequential data $\mathbf{x}_t$ is encoded through $g_{enc}(\mathbf{x}_t) = \mathbf{z}_t$ and aggregated over previous encodings through auto-regressor $g_{ar}(\mathbf{z}_1 \dots \mathbf{z}_t) = \mathbf{c}_t$, where both $\mathbf{z}_t$ or $\mathbf{c}_t$ may serve as representations for downstream tasks. The encoder function $g_{enc}(\cdot)$ is usually represented by a ConvNet, and $g_{ar}(\cdot)$ by a Gated Recurrent Unit (GRU). Finally, the encoding functions $g_{enc}(\cdot)$ and $g_{ar}(\cdot)$ are obtained by optimising a global loss function, the InfoNCE loss, end-to-end via backpropagation.

Instead, in this study, we split up $g_{enc}(\cdot)$'s network architecture by depth into M modules

$$g^1_{enc}(\cdot),\ g^2_{enc}(\cdot),\ \dots,\ g^M_{enc}(\cdot)$$

and prevent gradients from flowing between modules, as introduced in GIM. An additional optional $M+1$'th module $g_{ar}(\cdot)$ can be appended to the architecture. Each module is greedily optimised via a novel loss function, $\mathcal{L}_{\text{V-NCE}}$, which we will define in section 3.3. Each module's output serves as input for the successive module, as presented in the following equations.

$$\begin{aligned} g^1_{enc}(\mathbf{x}_t) &= \mathbf{z}^1_t \\ g^m_{enc}(\mathbf{z}^{m-1}_t) &= \mathbf{z}^m_t \\ g_{ar}(\mathbf{z}^M_1 \ \dots \ \mathbf{z}^M_t) &= \mathbf{c}_t \end{aligned}$$

The final representation $\mathbf{z}^M_t$ is obtained by propagating $\mathbf{x}_t$ through each modules as follows:

$$g^M_{enc}(\dots g^2_{enc}(g^1_{enc}(\mathbf{x}_t))) = \mathbf{z}^M_t$$

Additionally, taking inspiration from VAEs, the outputs from $g^m_{enc}(\cdot)$ and $g_{ar}(\cdot)$ are in fact samples from a distribution denoted by $q(\mathbf{z}^m_t \mid \mathbf{z}^{m-1}_t)$, defined as a multivariate Gaussian with diagonal covariance matrix, as follows:

$$q(\cdot \mid \mathbf{z}^{m-1}_t) = \mathcal{N}(\boldsymbol{\mu}, \text{diag}(\boldsymbol{\sigma}^2)) \tag{3.1}$$

with $\boldsymbol{\mu}$ and $\boldsymbol{\sigma}$ dependent on $\mathbf{z}_t^{m-1}$. The outputs for $g_{enc}^m(\cdot)$ and $g_{ar}(\cdot)$ are obtained by sampling from this distribution, denoted respectively, as follows:

$$\mathbf{z}_t^m \sim \ q^m(\cdot \mid \mathbf{z}_t^{m-1}) \tag{3.2}$$

$$\mathbf{c}_t \sim \ q^{M+1}(\cdot \mid \mathbf{z}_t^{M}) \tag{3.3}$$

We call these distributions the *posterior* distributions. Modules are thus stochastic and computing $g_{enc}^m(\mathbf{z}_t^{m-1})$ twice will likely result in two different representations of $\mathbf{z}_t^m$. This is in contrast to CPC and GIM's latent representations which remain fixed depending on the input (van den Oord et al., 2019; Löwe et al., 2020).

We achieve these stochastic modules by defining each module $g_{enc}^m(\cdot)$ consisting of two blocks. The first block receives as input $\mathbf{z}_t^{m-1}$ and predicts the parameters $\boldsymbol{\mu}$ and $\boldsymbol{\sigma}$, which fully describe the distribution $q^m(\cdot \mid \mathbf{z}_t^{m-1})$ defined in equation 3.1. The second block samples $\mathbf{z}_t^m \sim q^m(\cdot \mid \mathbf{z}_t^{m-1})$ from this distribution and produces an output representation. This is depicted in figure 3.1.

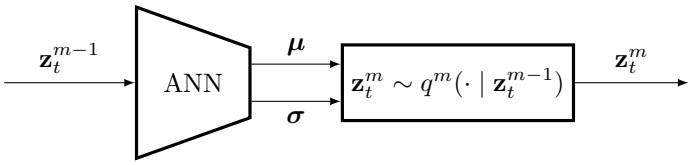

Figure 3.1: A single module.

In practice, sampling from q^m is achieved through a reparametrisation trick, as introduced in (Kingma and Welling, 2022). The equation to compute $\mathbf{z}_t^m$ then becomes:

$$\mathbf{z}_t^m = \boldsymbol{\mu} + \boldsymbol{\sigma} \odot \boldsymbol{\epsilon}$$

where $\boldsymbol{\epsilon}$ corresponds to a sampled value $\boldsymbol{\epsilon} \sim \mathcal{N}(\mathbf{0}, \mathbf{I})$ and $\odot$ is element-wise multiplication. The procedure to obtain $\mathbf{c}_t$ is analogous to $\mathbf{z}_t^m$.

3.3 The Loss Function

Instead of training the neural network's modules end-to-end with a global loss function, each module is optimised greedily with its own personal loss function. Through the introduction of the novel *Variational-InfoNCE* loss, mutual information between temporally nearby representations is maximised, while regularising the latent space to be approximate to the standard Gaussian $\mathcal{N}(\mathbf{0}, \mathbf{I})$. The Variational-InfoNCE loss is defined as follows:

$$\mathcal{L}^m_{\text{V-NCE}} = \underbrace{\sum_k \mathop{\mathbb{E}}_{\substack{\mathbf{z}^m_{t+k} \sim q^m(\cdot \mid \mathbf{z}^{m-1}_{t+k}) \\ \mathbf{z}^m_t \sim q^m(\cdot \mid \mathbf{z}^{m-1}_t)}} \left[\log \frac{f_k^m(\mathbf{z}^m_{t+k}, \mathbf{z}^m_t)}{\sum_{\mathbf{z}^m_j \in X} f_k^m(\mathbf{z}^m_j, \mathbf{z}^m_t)} \right]}_{\text{Maximise } I(\mathbf{z}^m_{t+k}, \mathbf{z}^m_t)} + \underbrace{\beta \; D_{KL}\left(q^m(\cdot \mid \mathbf{z}_t^{m-1}) \;||\; \mathcal{N}(\mathbf{0}, \mathbf{I})\right)}_{\text{Regularisation}} \tag{3.4}$$

Here, $m \in \mathbb{N}$ refers to the m'th module and $k \in \mathbb{N}$ the number of patches in the future the similarity score $f_k^m(\mathbf{z}^m_{t+k}, \mathbf{z}^m_t)$ must rate. The latent representations $\mathbf{z}^m_{t+k}$ and $\mathbf{z}^m_t$ are encoded samples produced by $g^m_{enc}(\mathbf{z}^{m-1}_{t+k})$ and $g^m_{enc}(\mathbf{z}^{m-1}_t)$, respectively and X is a set of samples $\left\{\mathbf{z}^m_{t+k}, \mathbf{z}^m_1, \mathbf{z}^m_2, \dots\right\}$ where $\mathbf{z}^m_j$ with $j \neq t+k$ are random samples.

The similarity score $f_k^m(\cdot)$'s definition is identical to (Löwe et al., 2020):

$$f_k^m(\mathbf{z}_{t+k}^m, \mathbf{z}_t^m) = \exp({\mathbf{z}_{t+k}^m}^T W_k^m \mathbf{z}_t^m)$$

$\mathcal{L}_{\text{V-NCE}}^m$ consists of two terms. The first term ensures that latent representations of temporally nearby patches contain maximised mutual information. The second pushes the latent representations close to the origin. Finally, β is a hyper-parameter which decides the relative importance between the two terms. $\beta >> 1$ will weight more importance to regularisation but may result in posterior collapse (Lucas et al., 2022). On the other hand, $\beta \approx 0$ will put more importance to the mutual information maximisation term while forgetting about the regularisation term. When $\beta = 0$, V-GIM is identical to GIM but with an altered neural network architecture which supports probabilistic latent representations.

3.3.1 The Gradient

To estimate the expectation term in $\mathcal{L}_{\text{V-NCE}}$, we apply the same approximation method as in VAEs, achieved through Monte Carlo estimates (Kingma and Welling, 2022). The first term $\mathcal{L}_{\text{V-NCE}}$ in then becomes:

$$\sum_k \frac{1}{L} \left[\sum_{l=1}^{L} \log \frac{f_k^m({\mathbf{z}_{t+k}^m}^{(l)}, \mathbf{z}_t^{m(l)})}{\sum_{\mathbf{z}_j^m \in X} f_k^m(\mathbf{z}_j^m, \mathbf{z}_t^{m(l)})} \right]$$

Here, L refers to the number of samples drawn for a single data point and each ${\mathbf{z}_{t+k}^m}^{(l)}$ or $\mathbf{z}_t^{m(l)}$ is a different sample. However, as argued by Kingma and Welling, choosing a large batch size will allow this value to be set to 1 without harming performance (Kingma and Welling, 2022).

With regards to the second term, since $q^m(\cdot \mid \mathbf{z}_t^{m-1})$ is a Gaussian defined by parameters $\boldsymbol{\mu}$ and $\boldsymbol{\sigma}$, a closed-form solution exists (Kingma and Welling, 2022). The closed form equation is the following:

$$D_{KL}\left(q^m(\cdot \mid \mathbf{z}_t^{m-1}) \,||\, \mathcal{N}(\mathbf{0}, \mathbf{I})\right) = \frac{1}{2} \sum_{k=1}^{D} \left(-\log \sigma_k^2 - 1 + \sigma_k^2 + \mu_k^2\right)$$

Therefore, this term can be directly computed and does not need to be approximated through Monte Carlo. The gradient for the two terms can then be computed using an automatic differentiation tool such as PyTorch (Paszke et al., 2017).

3.3.2 Properties of the Latent Space

In this section, we present two important conjectures regarding the structure of the latent space defined by each of V-GIM's modules. For each module $g_{enc}^m(\cdot)$ (or analogously for $g_{ar}(\cdot)$), an input space $\mathcal{Z}^{m-1}$ is mapped to a latent space $\mathcal{Z}^m$ as follows:

$$g_{enc}^m : \mathcal{Z}^{m-1} \to \mathcal{Z}^m$$

Here, $\mathcal{Z}^0$ equals the feature space $\mathcal{X}$. The two conjectures hold true when $\mathcal{L}_{\text{V-NCE}}$ is optimal. They will serve as the main argument for why V-GIM's representations are interpretable, discussed in section 3.4. Meanwhile, traditional techniques such as CPC and GIM lack these interpretable benefits.

Conjecture 1: $\mathcal{Z}^m$ is uninterrupted and well-covered around the origin.

In V-GIM, a latent representation $\mathbf{z}_t^m \in \mathcal{Z}^m$ of a data point $\mathbf{z}_t^{m-1} \in \mathcal{Z}^{m-1}$ is a sample from the Gaussian distribution $q^m(\cdot \mid \mathbf{z}_t^{m-1})$. Thus, encoding the same $\mathbf{z}_t^{m-1}$ an infinite number of times results in an entire spherical region (around a particular mean $\boldsymbol{\mu}$) in $\mathcal{Z}^m$ that is entirely covered by the latent representations corresponding to $\mathbf{z}_t^{m-1}$, without any interruptions in this region. This is different from GIM and CPC where a data point merely covers a single point of the latent space (and not an entire region). Furthermore, because each region should be close to the origin, regions are more likely to utilise the limited space efficiently around the origin, resulting in a lower chance of obtaining large holes between two regions from different data points. As a result, the latent representations from the dataset should cover the entire latent space around the origin, such that all latent representations around the origin have a corresponding data point that is similar to a data point from the dataset.

Conjecture 2: $\mathcal{L}_{\text{V-NCE}}$ enforces smooth and consistent transitions in the latent space with respect to the mutual information of the original data points.

As we discussed in section 3.3, the first term in $\mathcal{L}_{\text{V-NCE}}$ maximises the mutual information $I(\mathbf{z}_t^m, \mathbf{z}_{t+k}^m)$, which was proven by van den Oord et al. (2019). However, in addition, Löwe et al. (2020) argue that when modules are trained in a greedy setting using this loss function, the mutual information between outputs of successive modules $I(\mathbf{z}_t^{m-1}, \mathbf{z}_t^m)$ is also maximised, and therefore also $I(\mathbf{x}_t, \mathbf{z}_t^m)$. Or equivalently, given a data point $\mathbf{x}_t^{(i)}$, the output produced by $g_{enc}^m(\dots g_{enc}^2(g_{enc}^1(\mathbf{x}_t^{(i)}))) = \mathbf{z}_t^m$ will ensure $I(\mathbf{x}_t^{(i)}, \mathbf{z}_t^m)$ to be maximum. This is an important observation. Now, since the latent representations corresponding to $\mathbf{x}_t^{(i)}$ cover an entire spherical region (as discussed in conjecture 1), the mutual information $I(\mathbf{x}_t^{(i)}, \mathbf{z}_t^m)$ for all the latent representations $\mathbf{z}_t^m$ in this region should be maximised.

Let us now consider a second data point $\mathbf{x}_t^{(j)}$ whose corresponding regions in $\mathcal{Z}^m$ overlap with $\mathbf{x}_t^{(i)}$'s region. Since regions are fairly large and the latent space is small, this is likely to happen. Due to the overlap between the regions, there exists a latent representation $\mathbf{z}_t^{m\prime}$ that corresponds to both $\mathbf{x}_t^{(i)}$ and $\mathbf{x}_t^{(j)}$. Since $\mathbf{z}_t^{m\prime}$ is lower dimensional and is defined such that $I(\mathbf{z}_t^{m\prime}, \mathbf{x}_t^{(i)})$ and $I(\mathbf{z}_t^{m\prime}, \mathbf{x}_t^{(j)})$ are both maximised, $\mathbf{z}_t^{m\prime}$ contains information that is common to both $\mathbf{x}_t^{(i)}$ and $\mathbf{x}_t^{(j)}$ (if not, $\mathbf{z}_t^{m\prime}$ would not have been in the two regions).

If small changes to the components of $\mathbf{z}_t^{m\prime}$ caused abrupt changes in the corresponding feature vectors in $\mathcal{X}$, this would be heavily penalised by $\mathcal{L}_{\text{V-NCE}}$ due to the width of the Gaussian regions. Therefore, the transitions in the latent space must be smooth to ensure that small changes in $\mathbf{z}_t^{m\prime}$ lead to small changes in the corresponding feature vectors in $\mathcal{X}$.

Furthermore, due to the definition of q^m with covariance matrix containing only non-zero values on the diagonal, the components of q^m are independent. Therefore, moving a latent representation in a single direction of a particular dimension should cause the same effect on the mutual information with respect to the corresponding data point in $\mathcal{X}$ as moving it in a different dimension. This property ensures that the transitions in the latent space are consistent.

Finally, the result of these two conjectures is an uninterrupted latent space around the origin where moving a latent representation towards a particular dimension in the latent space causes smooth and consistent changes in the corresponding data point from the previous module's latent space. This crucial observation will serve as the main argument for why V-GIM's representations are interpretable, while traditional techniques such as CPC and GIM do not have these guarantees.

3.4 Computational Benefits

Each module in V-GIM is greedily trained through the variational InfoNCE loss. This approach, as suggested by Löwe et al. (2020), offers several computational benefits, including decoupled and asynchronous distributed training. Modules can then be trained in parallel on multiple devices, or sequentially on a single device. This is particularly interesting for memory-constrained devices, as it enables the training of architectures that exceed the available memory capacity. Furthermore, V-GIM mitigates the vanishing gradient problem, a well-known issue in deep architectures, by preventing the flow of gradients between modules (Hu et al., 2021).

In addition to the benefits associated with greedy training, V-GIM adds a constraint to the latent space produced by each module, resulting in further practical benefits. Since V-GIM adopts a greedy training approach, these benefits apply not only to the final module's output but also to the outputs of intermediate modules.

Interpretability of final and intermediate modules

By regularising the latent space resulting in the properties discussed in section 3.3.2, each of V-GIM's modules define a space where sampling from a point around the origin is likely to correspond to a data point that is similar to the dataset. A decoder trained on this space will generalise well to unseen data when given a latent representations around the origin. This has significant implications for V-GIM's interpretability. Not only can we assess the information contained in a latent representation through a decoder, but we can also attempt to understand the underlying structure of the latent representation. This is achieved in a similar way as with VAEs, where manipulating a individual dimension's value and observing the effect through the decoder gives insight into the specific information contained in that dimension.

Furthermore, since V-GIM's neural network architecture consists of a variable number of modules, each with its own interpretable latent space, these benefits are applicable to the latent representations produced by intermediate modules, allowing us to observe the internal mechanism of the neural network. Additionally, since convolution layers in ConvNets typically reduce the length of representations, different modules encode different sequence lengths, encouraging different abstractions to be learned at different levels. By having intermediate modules be interpretable, we can analyse these abstractions as well. This is in contrast to VAEs, where only the output latent representation is interpretable, and intermediate representations in the architecture are not.

In contrast, GIM and CPC do not pose constraints on the latent space. Although a decoder can still be trained on the latent representations of GIM and CPC, the latent space is highly unpredictable. Consequently, it is not guaranteed that the reconstructed output from a randomly sampled latent representation will be meaningful, as it may be very dissimilar from the original data. Moreover, attempting to decode an interpolated representation from two existing latent representations may not lead to a meaningful output either, since the latent space the decoder was trained on may contain large gaps. This makes it challenging to interpret the underlying structure of the latent representations defined by CPC and GIM.

Disentanglement

In section 2.3.2 on β-VAEs and disentanglement, Higgins et al. (2022) argue that setting the prior $p(\mathbf{z})$ to an isotropic Gaussian encourages disentanglement in the encodings. When encodings are fully disentangled, this results in each dimension from the encoding capturing a different property of the original data. Since $\mathcal{L}_{\text{V-NCE}}$ enforces the latent space to be standard normal, this theorem

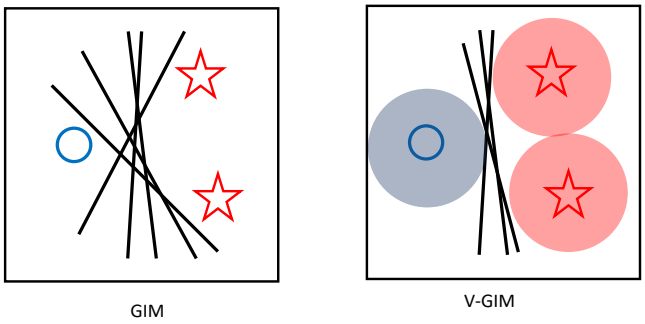

Figure 3.2: Example of a two-dimensional space obtained from GIM and V-GIM respectively, where a binary classifier is given three data points. The black lines represent all the possible decision boundaries, while the circular areas in V-GIM represent the samples obtained from the corresponding Gaussian distribution.

is also applicable to V-GIM and choosing a large value for β in $\mathcal{L}_{\text{V-NCE}}$ applies more pressure for encodings to be disentangled further increasing interpretability.

Improved generalisation performance through representation variance

V-GIM's encodings are samples from a distribution, which means that a single patch of data $\mathbf{x}_t$ has multiple encoded representations $\mathbf{z}_t^M$. For downstream tasks with little labelled data, the variability in representations could serve as an internal data augmentation method, making the set of plausible decision boundaries smaller, and therefore also improving generalisation to unseen data. This motivation is further depicted in figure 3.2 where a two-dimensional latent space and the set of its plausible decision boundaries are shown.

Internal batch normalisation mechanism

During the training of ANNs, the weights of different layers undergo changes, which can lead to a problem known as "internal covariate shift" (Ioffe and Szegedy, 2015). This shift causes the distributions of each layer's input to change over time, which in turn can negatively affect subsequent layers, slowing down the training process (Bjorck et al., 2018; LeCun et al., 1998). This issue is typically addressed via batch normalisation (Santurkar et al., 2018; Bjorck et al., 2018), a mechanism which normalises the activations of internal layers, allowing for a higher learning rate during training and thus accelerating the process.

Batch normalisation is especially important in a greedy setting such as GIM and V-GIM, where modules are independently trained in parallel. Without intermediate normalisation, subsequent modules may learn slower than previous modules, resulting in the subsequent modules not being able to catch up in time to the changes from preceding modules made during training. The result would be that modules may have to be trained with different learning rates, resulting in an additional hyperparameter that must be obtained for each module.

In contrast, V-GIM already contains an internal normalisation mechanism in-between modules. This is indirectly caused by regularising each module's latent space to have a zero-mean and standard deviation of one. Finally, the normalised encodings can also be beneficial for downstream tasks. If normalisation is desired, computing the mean and standard deviation over a potentially very large dataset is not required, as this is already built into the encodings.

Chapter 4

Experiments

In this chapter, we evaluate the effectiveness of the latent representations obtained from Variational Greedy InfoMax (V-GIM) in comparison to its non-variational counterpart, GIM, by training both models on sequential data from the audio domain. To assess the quality of the representations, we project them into a two-dimensional space using t-SNE and analyse the emergence of potential clusters. Moreover, we use a linear classifier that takes these representations as input and evaluate its accuracy to gain insights into the performance of these models. To further examine the efficacy of these representations, we investigate their potential for downstream task generalisation by training the linear classifier on smaller subsets of the dataset and assessing the amount of labelled data required to achieve satisfactory performance. Finally, we delve into the underlying structure of V-GIM's representations by training a decoder on top of each of V-GIM's modules, providing insights into their composition.

4.1 Experimental details GIM and V-GIM

GIM and V-GIM are trained on raw speech signals of fixed length sampled at 16 kHz. The dataset consists of 851 audio files and is randomly shuffled and split up into 80% training data (680 files) and 20% test data (171 files). Each audio file consists of a single spoken sound consisting of three consonants and three vowels, where the consonants and vowels alternate with each other. Some examples are the sounds "gi-ga-bu" and "ba-bi-gu". The words consist of three syllables from the following list: ba, bi, bu, da, di, du, ga, gi and gu. All the sounds are spoken by the same person, in a constant and peaceful tone. We crop the files to a fixed length of 10240 samples, or 640 milliseconds, which is slightly longer than half a second.

GIM and V-GIM are trained on the same architecture, consisting of two encoder modules $g^1_{enc}(\cdot)$ and $g^2_{enc}(\cdot)$, no autoregressive module $g_{ar}(\cdot)$ is used. The modules are trained in parallel. Each module consists of solely convolution and pooling layers. Since the architecture contains no fully connected layers, the length of the audio files can therefore be variable during inference. The architecture details for the two modules are presented in tables 4.1 and 4.2. ReLu non-linearity is applied after each convolution layer, except in the last layer in each module. No batch normalisation is used. The number of hidden channels produced by each convolution and pooling layer remains constant, at 32 channels. In each module, data flows synchronously from one layer to the successive layer, except in the final two layers. These run in parallel and both take the same input from the preceding layer. This architecture choice is related to the parametrisation trick we discussed in section 3.2. One layer generates $\boldsymbol{\mu}$ and the other $\boldsymbol{\sigma}$ such that $\mathbf{z}^m_t$ can be computed via the reparametrisation trick. The architecture is visualised in figure

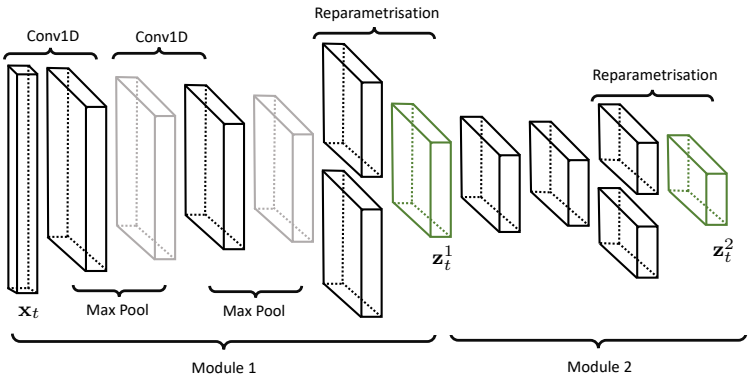

Figure 4.1: Visualisation of V-GIM's architecture.

4.1. An input signal of length 1×10240 is downsampled to 32×52 by the first module and to 32×13 by the second module. Taking overlap into consideration, each latent representation $\mathbf{z}_t^M = \mathbf{z}_t^2$ captures 64ms of speech.

Layer	**Kernel Size**	**Stride**	**Padding**
Conv1D	10	4	2
Max Pool	8	4	0
Conv1D	8	3	2
Max Pool	8	4	0
In parallel:			
Conv1D	3	1	2
Conv1D	3	1	2

Table 4.1: Module 1 architecture.

Layer	**Kernel Size**	**Stride**	**Padding**
Conv1D	6	2	2
Conv1D	6	2	2
In parallel:			
Conv1D	3	1	1
Conv1D	3	1	1

Table 4.2: Module 2 architecture.

Importantly, the reparametrisation trick is included in our implementation of GIM's architecture as well. However, by enforcing no constraints on the latent space, which is achieved by assigning $\beta = 0$ in $\mathcal{L}_{\text{V-NCE}}$, we observed that $\boldsymbol{\sigma}$ moves towards $\mathbf{0}$ such that all the randomness from sampling from a Gaussian distribution is removed. As such, our implementation of GIM is equivalent to GIM introduced in (Löwe et al., 2020) but with an altered architecture.

Both GIM and V-GIM are trained using the Adam optimiser for 800 epochs with an exponential learning rate scheduler (Bhargav Lad, 2020), with initial learning rate $lr_{init} = 0.01$ and $\gamma = 0.995$, such that lr is updated as follows:

$$lr_{epoch} = \gamma * lr_{epoch-1}$$

The batch size is set to 171, which is exactly the size of the test set. The number of patches to predict in the future k, is set to 12. Implementation details with regards to drawing negative samples for $f_k^m(\cdot)$ remain identical to the experiments from (van den Oord et al., 2019) and (Löwe et al., 2020). The regularisation importance term β is set to 0 for GIM and 0.0035 for V-GIM, which is the largest value we could obtain without causing posteriors to collapse to the standard normal, commonly referred to as posterior collapse.

After training V-GIM and GIM for 800 epochs, we train linear multi-class classifiers for 100 epochs on their respective latent representations for every module, evaluated using Cross-Entropy (Ho and Wookey, 2020). We set $lr = 0.001$ and use the Adam optimiser without scheduler. The classifier is tasked to predict the syllable corresponding to its latent representation. Details on the algorithm used to split up audio files by individual syllables are provided in appendix A. Speech waves are zero-padded at both the beginning and the end to achieve a fixed length between syllables. The corresponding latent representations thus all consist of a fixed number of time frames $\mathcal{T}$ and 32 channels. Here, $\mathcal{T}$ is different depending on the depth of the module. The classifier consists of a single connected layer with $32 \times \mathcal{T}$ input nodes and 9 output nodes, matching the number of input features and the number of classes respectively. We reshuffle the dataset and use 80% for training and 20% for testing.

4.2 Results GIM and V-GIM

4.2.1 Training Error

Figure 4.2 displays the loss curves corresponding to GIM ($\beta = 0$) and V-GIM ($\beta = 0.0035$) for both modules. In the first module, the test loss for GIM is lower compared to V-GIM. This is expected because V-GIM includes an additional regularisation term in its loss function. In the second module, both GIM and V-GIM have loss curves that converge to lower values than their previous module. This suggests that the task becomes easier for the subsequent modules, indicating that the preceding module does indeed make simplified representations of the speech data.

Interestingly, in the second module, V-GIM has a lower loss compared to GIM, even though V-GIM includes the regularisation term in its loss function. We argue that this is related to internal covariate shift, which we discussed in section 3.4. Using a relatively large learning rate for GIM and V-GIM leads to a significant "drift" in the distribution of activations during training, making it difficult for GIM's successive modules to keep up with these changes. V-GIM is less susceptible to this issue due to the internal batch-normalisation mechanism that is built into the regularisation term. Consequently, V-GIM's modules can train with a larger learning rate without affecting the performance of successive modules, resulting in faster convergence.

4.2.2 t-SNE

We project the latent representations obtained from each module to a two-dimensional plane using t-SNE (van der Maaten and Hinton, 2008). This enables us to observe potential clusters, as similar data points are mapped close together, while dissimilar points remain far away. Similar to the syllable classifier discussed in section 4.1, t-SNE is trained on flattened representations that are split into individual syllables, without performing any pooling. We run t-SNE with random initialisation, perplexity of 30 and a learning rate of 200 for 1000 iterations.

The graphs for GIM and V-GIM are displayed in figure 4.3. T-SNE was not provided with any information about the class labels. Syllables containing the vowel "a" are represented with a red tint, "u" with green, and "i" with blue. We observe similar results in the first module of both GIM and V-GIM. T-SNE identifies two clusters, with one cluster corresponding to syllables containing an "a" and the other cluster to containing "u" or "i". Within the "u/i" cluster, there is still a grouping of "u" and "i" data points. However, distinguishing between "b", "d" or "g" is more challenging as data points within the clusters are entangled.

In the second module, we observe more significant differences between GIM and V-GIM. In V-GIM's second module, there is a clearer separation between the "i" and "u" syllables, indicating

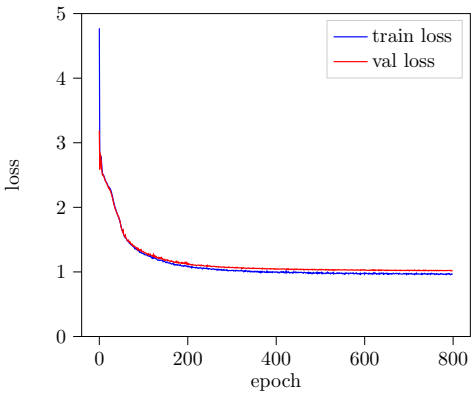

(a) Module 1: $\beta = 0.0035$

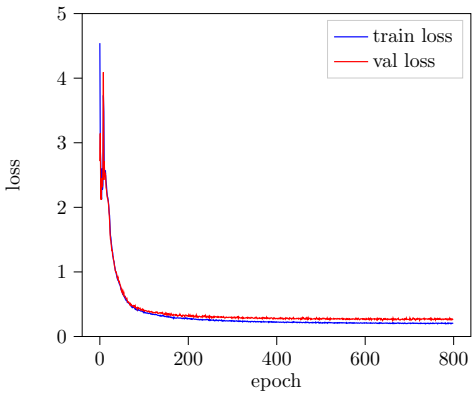

(b) Module 2: $\beta = 0.0035$

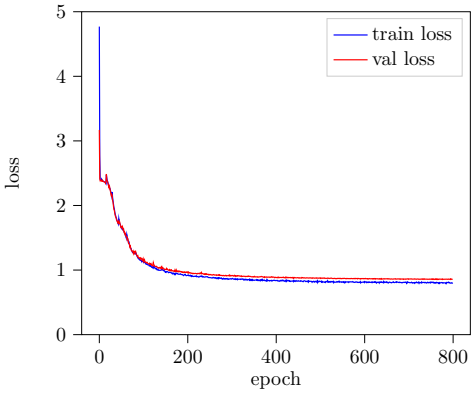

(c) Module 1: $\beta = 0$

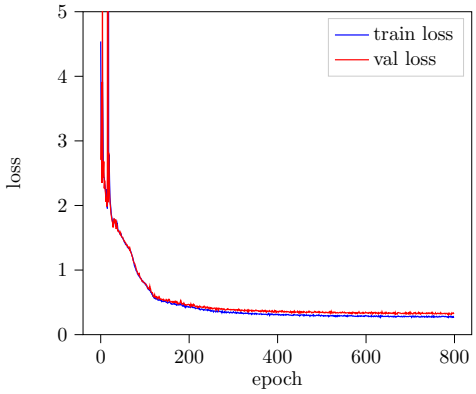

(d) Module 2: $\beta = 0$

Figure 4.2: Training and validation loss (GIM: $\beta = 0$, V-GIM: $\beta = 0.0035$).

that the second module contributes to improved latent representations. However, distinguishing between pronounced consonants remains difficult. On the other hand, GIM's second module does not appear to have converged well, as t-SNE struggles to separate the representations into meaningful clusters. Consequently, syllables are mixed without much structure. This further emphasises how GIM is affected by internal covariate shift, while V-GIM is not.

4.2.3 Classification Performance

Table 4.3 presents the accuracies of the linear classifier, which aims to predict the syllable corresponding to the latent representation. There are a total of 9 different syllables, such that a random model would obtain an accuracy of 11%. While the t-SNE plots in figure 4.3 have demonstrated that vowels can be distinguished relatively easily, differentiating consonants poses a greater challenge. As a result, both GIM and V-GIM show mediocre test accuracies, ranging between 53% and 54% in the first module, and further decreasing in the second module. These accuracy values, coupled with the t-SNE plots, indicate that information regarding the consonants may no longer be adequately captured in GIM and V-GIM's latent representations. Moreover, the performance continues to decline when considering the accuracies obtained from the two second modules.

Method	Accuracy Module 1 (%)	Accuracy Module 2 (%)
GIM	53.68 ± 1.82	30.09 ± 1.87
V-GIM	50.78 ± 1.87	41.7 ± 1.54

Table 4.3: Accuracies obtained on the test dataset. The values are calculated based on 5 repetitions.

We believe that these mediocre accuracies can be attributed to the limited mutual information between temporally nearby patches. GIM and V-GIM assume data that adheres to the slowly changing features assumption, which is necessary to maximise the mutual information between the latent representations of temporally nearby data patches. Consequently, abrupt changes in the patches are discarded from the latent representations. However, in general, the words spoken in the dataset consist of longer durations for vowels compared to consonants. For instance, in the syllable "ba", the phoneme "b" is usually pronounced for a shorter duration than the "a". This can cause a problem when the phone "b" is not captured over multiple patches, as only the mutual information between the patches is kept. Additionally, latent representations are optimised to maximise the mutual information with the future k patches. Since k remains fixed over the different modules and deeper modules capture longer time windows, the latent representations of deeper modules must capture more information, while the number of channels remains relatively small, at 32.

4.2.4 Distributions

Figures 4.4, 4.5, 4.6 and 4.6 depict the distributions of activations corresponding to an individual dimension. Each sub-figure depicts the distributions for a single module. We display the distributions for the first six dimensions. We observe that V-GIM does indeed learn to constrain the latent space to the standard normal for most dimensions. Meanwhile, in GIM's first module, we observe high and thin peaks, indicating that the same value is regularly predicted with little noise due to $\boldsymbol{\sigma} \approx 0$. The peaks are less dominant in the second module, which may be attributed to suboptimal convergence.

4.3 Generalisation Study

In contrast to GIM, V-GIM's latent representations are samples from a distribution, resulting in a single patch of data having multiple latent representations. In this section, we examine whether a linear classifier with little annotated training data can benefit from this representation variability introduced by V-GIM. We train multiple multi-class classifiers with the same experimental details as discussed in section 4.1 but with a modification to the annotated training set. Each classifier is trained on a subset of the dataset, varying between 1 data point per class, all the way up to 128 data points. The batch size is set to the size of the subset. Training details for GIM and V-GIM remain unchanged, including the size of the training set, which does not require any labels.

The test accuracies are shown in figure 4.8. Overall, we observe no performance benefit from V-GIM's representation variance. Performance in GIM and V-GIM's first modules remains consistent, regardless of the subset size. Meanwhile, differences in the second module are more prominent. However, this is related to the internal batch normalisation mechanism, discussed in section 4.2.1, resulting in faster convergence of V-GIM's modules.

4.4 V-GIM's Interpretability Analysis

In the following sections, we delve deeper into V-GIM's latent representations, aiming to gain an understanding of their captured information and understand their underlying structures. This is achieved by employing a decoder on top of each of V-GIM's modules. By altering the values of a representation in one dimension at a time and observing the effect through the decoder, we can analyse the contained information in each individual dimension. As we argued in section 3.4, this is only possible because V-GIM's latent space is optimised to be approximate to the standard normal. The decoder can then generalise to the altered representations as long as the representations are close to the origin.

4.4.1 Decoders for V-GIM

We employ two decoders, one for each module, which can be represented as follows: $D(\mathbf{z}_t^1) = \widetilde{\mathbf{x}}_t$ for the intermediate decoder and $D(\mathbf{z}_t^2) = \widetilde{\mathbf{x}}_t$ for the final decoder. This allows us to assess the information in both the final and the intermediate representations. Architecture details for the two decoders are provided in tables 4.4 and 4.5. An intermediate representation $\mathbf{z}_t^1$ with a shape of 32×1, capturing a single time step, is transformed into a speech signal $\widetilde{\mathbf{x}}_t$ with a shape of 1×448 (or 28ms). Similarly, the final representation $\mathbf{z}_t^2$ is transformed into a shape of 1×1024 (or 64ms).

Layer	**Kernel Size**	**Stride**	**Padding**
ConvTrans	3	1	1
ConvTrans	8	4	0
ConvTrans	8	3	2
ConvTrans	8	4	0
ConvTrans	10	4	2

Table 4.4: Decoder architecture for the intermediate latent representations.

Layer	**Kernel Size**	**Stride**	**Padding**
ConvTrans	3	1	1
ConvTrans	8	3	2
ConvTrans	8	3	2

Table 4.5: Decoder architecture for the final latent representations:

While the decoders can be optimised by minimising the Mean Squared Error (MSE) of the speech waves, this metric may not reflect well with the natural biases in human hearing. Humans perceive certain frequencies to be louder than others (Radkoff, 2021; Li et al., 2020). To account for this, we instead minimise the MSE on the mel-frequency spectrograms, which are an adaptation of linear spectrograms that emphasise frequency bins based on perceptual hearing biases (Shen et al., 2018). Additionally, we employ a logarithmic transformation to account for humans' logarithmic perceptual hearing (Braun and Tashev, 2020). Figure 4.9 illustrates an example of a log mel-spectrogram.

The loss function we use is the following:

$$\mathcal{L}_{\text{decoder}} = \frac{1}{n} \sum_{i=1}^{n} \left(\log(\text{MEL}(\mathbf{x}_t^{(i)})) - \log(\text{MEL}(\widetilde{\mathbf{x}}_t^{(i)})) \right)^2$$

In this equation, $\text{MEL}(\mathbf{x}_t^{(i)})$ represents the mel-spectrogram of the original signal $\mathbf{x}_t^{(i)}$, computed using the following parameters: the number of FFT bins set to 4096, the length of the hop between STFT windows set to 2048, and the number of filter banks set to 128. Other parameters are kept at their default values in PyTorch's MelSpectrogram implementation (Paszke et al., 2017). Logarithms in the equation are computed in base ten.

4.4.2 V-GIM Representation Analysis

Decoding latent representations into their original representation as a speech wave allows us to perceive the remaining information in the representation. It is worth mentioning that the reliability of this analysis is dependent on the performance of the decoder. If it is not able to reconstruct certain characteristics of the data, this does not necessarily mean the information is not contained in the latent representation.

Training and validation loss curves for both decoders are shown in figure 4.10. Overall, in both decoders, we observed that audio files could be reconstructed and the pronounced syllables were recognisable when listening to them. However, the reconstructed sounds were noisier and information about the speaker's identity was unrecognisable, suggesting that this information is either no longer contained in the latent representations, or the decoders are not able to replicate it. Additionally, while vowels were easily identifiable by listening to the audio, we observed that the decoder occasionally generated incorrect consonants. For instance, decoding the latent representation for "gu" could occasionally result in an incorrectly generated "bu" or "du". These observations are in line with the t-SNE plots and classification performance we discussed in the previous section, further suggesting that consonant information may no longer be present in the latent representations.

By decoding the latent representations of existing speech data, we gained insight into the remaining information in the representations. However, our goal goes further: we would like to also understand the underlying structure of these representations, and attempt to understand the precise information contained in each dimension. We achieve this by starting from the zero-vector $\mathbf{0}$ as latent representation and manipulating a single dimension at a time. We can then observe the effect in the reconstructed speech signals, by looking at it from the time and frequency domain. Figures 4.11, 4.12 and 4.13 show reconstructed speech signals, obtained from the *intermediate* decoder. We show the reconstructed audio waves, both in the time and frequency domain. In each figure, a single dimension is being manipulated, ranging between -2.68 and 2.68. Since the latent space is optimised to conform to the standard normal distribution, this would mean that 99% of the data points are contained within this range (Bhandari, 2020).

We suggest that the dimensions can be categorised into one of three groups based on their contained information. Figures 4.11, 4.12 and 4.13 show an example of each category. The first category contains information about frequencies for a specific frequency bin. Altering this dimension will a have a strong influence on the magnitude of one or two frequency bins, while other bins remain relatively unchanged. This is shown in figure 4.13, where changing the value of the 12th dimension towards -2.68 causes a peek around the 100 Hz frequency bin. The peek disappears when approaching 0. Meanwhile, when approaching +2.68, the magnitude of the 150 Hz frequency bin increases. Overall, we observed this kind of behaviour for roughly half of the 32 dimensions. The majority of dimensions were sensitive in the 100 Hz and 150 Hz frequency bins, while a few were in the 175 Hz bin. These ranges are to be expected as the pitch range for men's voices is between 60 and 180 Hz (Re et al., 2012).

Dimensions that belong to the second category, not only influence the magnitude of the frequencies in a specific bin, but also the neighbouring bins. In this category, modifying a dimension will cause an increase in the magnitude of a particular bin, while simultaneously influencing the surrounding frequencies. This results in a smooth envelope with a single peak which gradually decreases across the neighbouring bins. This behaviour is shown in figure 4.11.

The final category includes the dimensions which do not seem to make any contribution to the reconstructed signal. Changes to these cause very little change to the resulting speech wave, both in the time and frequency domain. These dimensions are either useless, or the decoder was not able to capture their contribution. An example is shown in figure 4.12.

Regarding the second decoder, which was trained with V-GIM's *final* representations, we observe that syllables are audible, but due to disturbances, it becomes more challenging to distinguish the precise syllables. This is to be expected, as latent representations in the second module capture speech sequences of a longer time frame (64ms instead of 28ms) while remaining the same size at 32 dimensions.

In the final representations, we observed more dimensions of the second category, containing the information of an entire neighbourhood of frequency bins, influencing frequencies ranging between 80 to 300 Hz. Additionally, we observed peaks in the frequency domain with much stronger magnitudes, compared to those in the intermediate representations. An example is shown in figure 4.14, displaying the reconstructed speech wave in the time and frequency domain for a final representation.

4.4.3 Vowel Experiment

To gain better insight into which dimensions incorporate vowel information, we train a linear classifier to predict whether the vowel corresponding to a syllable's latent representation is an "a", "i" or "u"[1]. Implementation details are the same as the linear classifier in section 4.1, but with only the three classes and without a bias term. The classifier is trained on the latent representations from V-GIM's first module. Additionally, representations are max pooled over the time domain, resulting in a single 32-dimensional feature vector for each syllable. After training, a Softmax function is appended to normalise predictions into probability values. After convergence, the classifier obtained a test accuracy of 85.38%.

Figure 4.15 displays the weights of the linear classifier. The weights are scaled between -1 and 1. Each row corresponds to the weights corresponding to an individual prediction class. Equivalently, when considering a graph representation for the classifier, the weights on the edges corresponding to a particular output node, are the values in a single row. Consequently, values close to 1 or -1 indicate a high (positive or negative) correlation between the target class and the corresponding dimension.

Interestingly, most dimensions appear to contribute very little to the predicted outcome, indicating that these dimensions are either useless, or the classifier did not find value in their contained information. Consequently, most vowel information can be derived with relatively high accuracy from merely a small subset of dimensions.

In addition, we observe that certain dimensions contain information for a single vowel, while others contain information for two. Values in the first dimension, for instance, have a strong correlation with the vowel "a", while no significant correlation with "i" or "u" appears to be present. Meanwhile, values in dimension 17 contain information for both "a" and "i", depending on whether the values approach 1 or -1.

Figure 4.16 displays the decision boundary that was learned by the consonant classifier. We observe relatively thin "grey zones" where the probabilities are not particularly decisive for a single consonant. For the majority of the data points in the latent space, the classifier thus makes predictions with relatively high certainty. In addition, the area corresponding to the prediction "u" is smaller than the other areas. This could potentially be explained as the sounds "a" and "i" can easily be distinguished, while the sound for "u" is somewhere in between, and thus harder to distinguish.

[1]The phoneme sounds a, i, and u are represented as [a], [i] and [u], respectively, in the international phonetic alphabet (IPA) (Teach Wonderful, 2021)

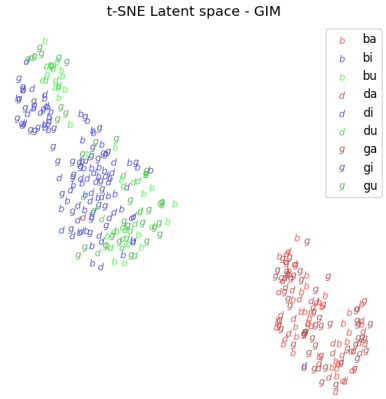

(a) Module 1: $\beta = 0.0035$

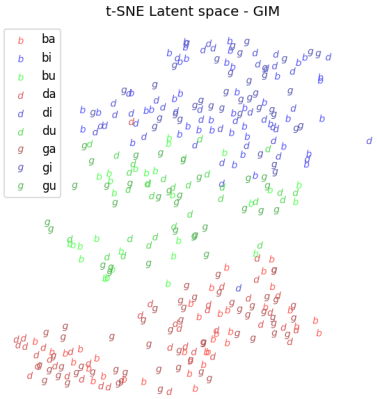

(b) Module 2: $\beta = 0.0035$

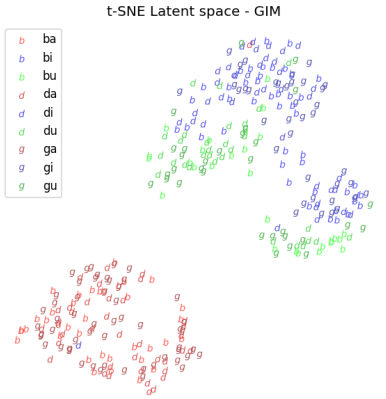

(c) Module 1: $\beta = 0$

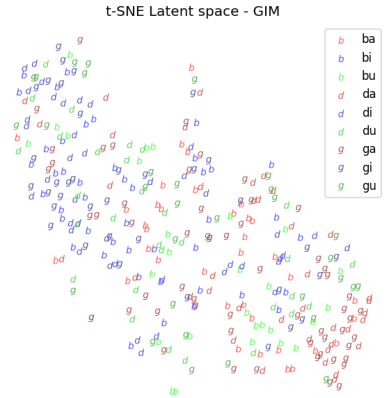

(d) Module 2: $\beta = 0.0035$

Figure 4.3: t-SNE plots (GIM: $\beta = 0$, V-GIM: $\beta = 0.0035$).

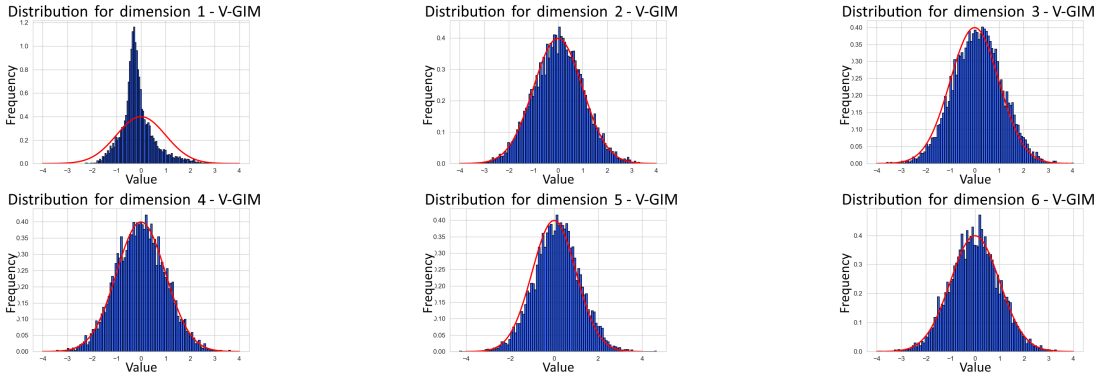

Figure 4.4: Histogram displaying how the latent points of a particular dimension are distributed. The latent points are obtained from V-GIM's *intermediate* module.

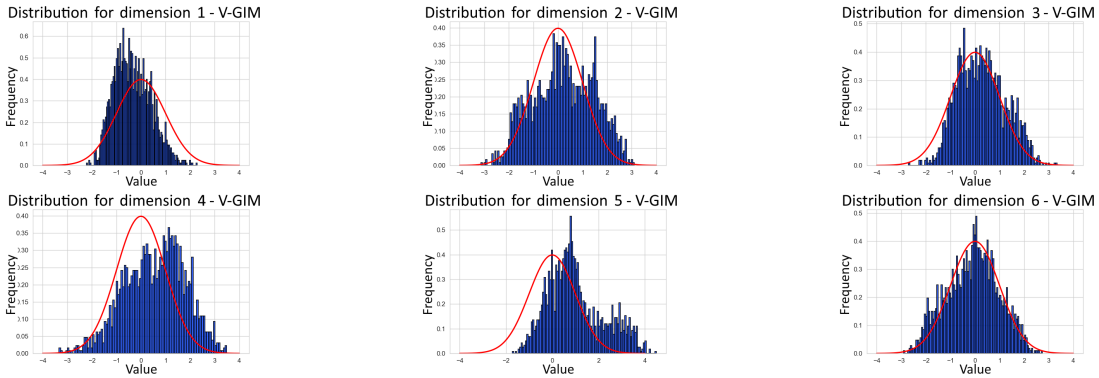

Figure 4.5: Histogram displaying how the latent points of a particular dimension are distributed. The latent points are obtained from V-GIM's *final* module.

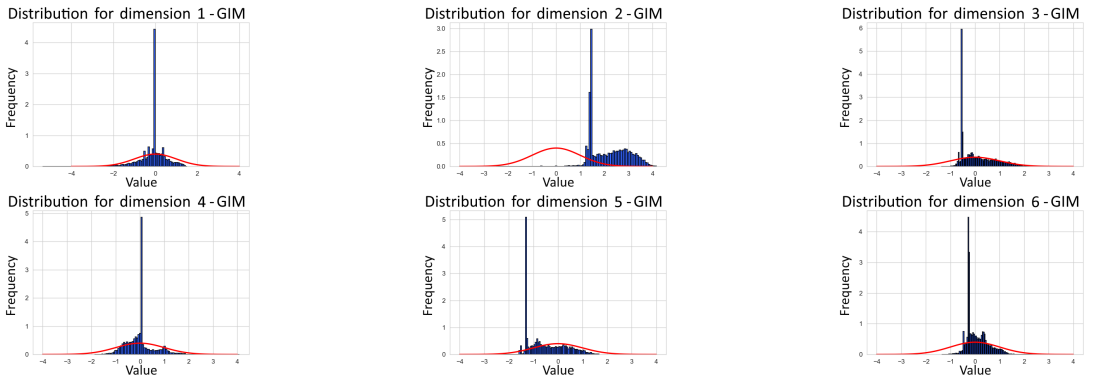

Figure 4.6: Histogram displaying how the latent points of a particular dimension are distributed. The latent points are obtained from GIM's *intermediate* module.

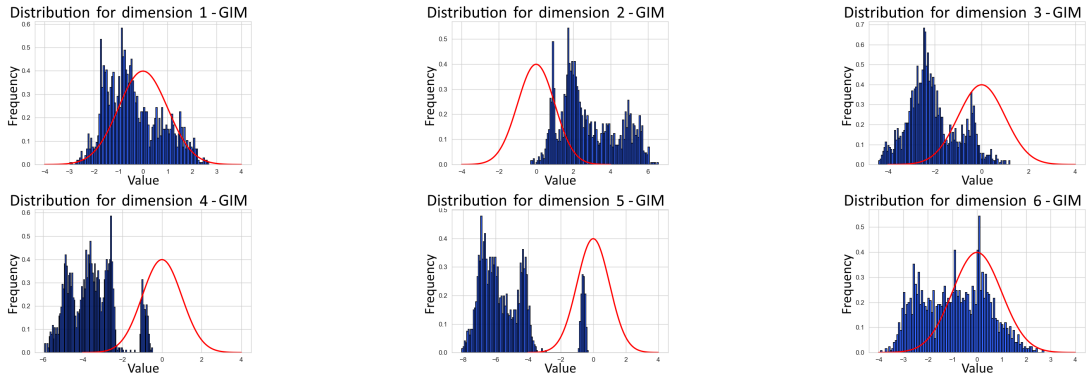

Figure 4.7: Histogram displaying how the latent points of a particular dimension are distributed. The latent points are obtained from GIM's *final* module.

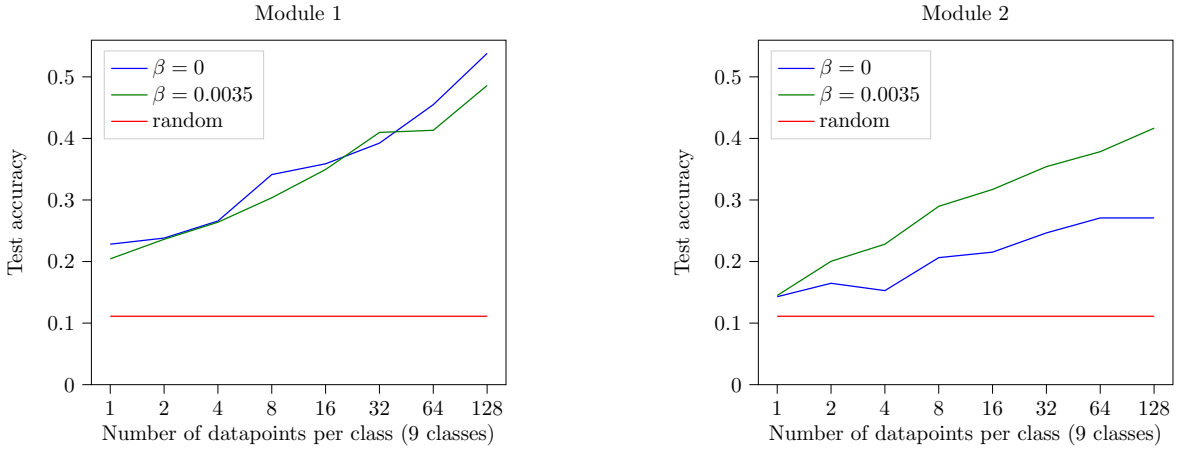

Figure 4.8: Test accuracy for different subset sizes.

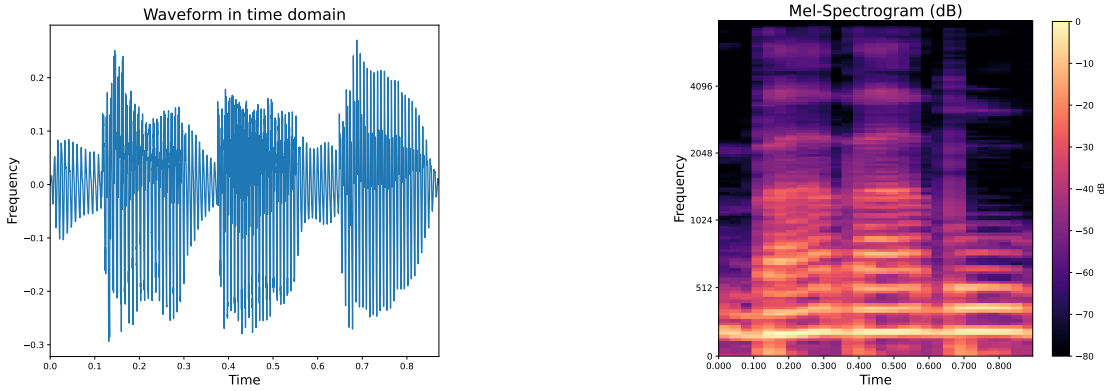

Figure 4.9: Example waveform and mel-spectrogram for "bababu".

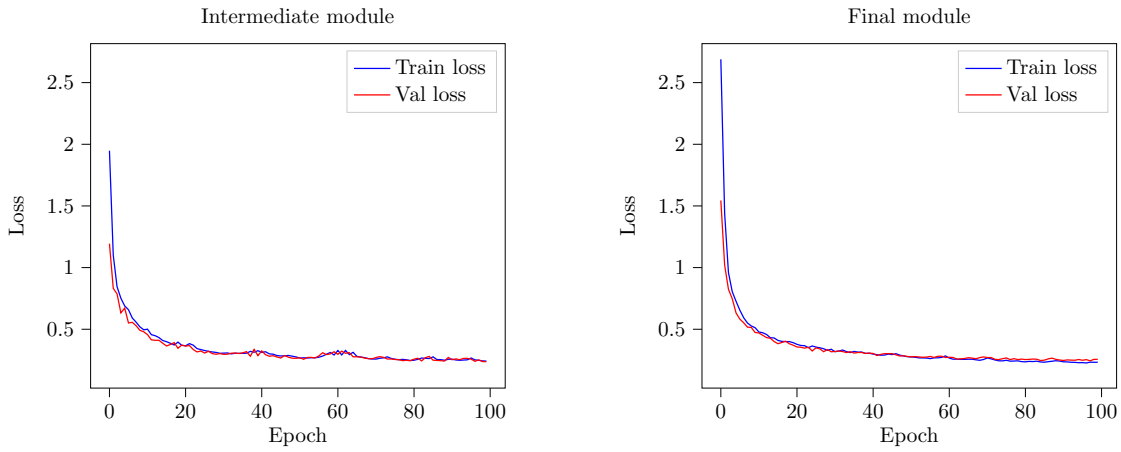

Figure 4.10: Training and validation loss for the two decoders, trained with V-GIM's representations.

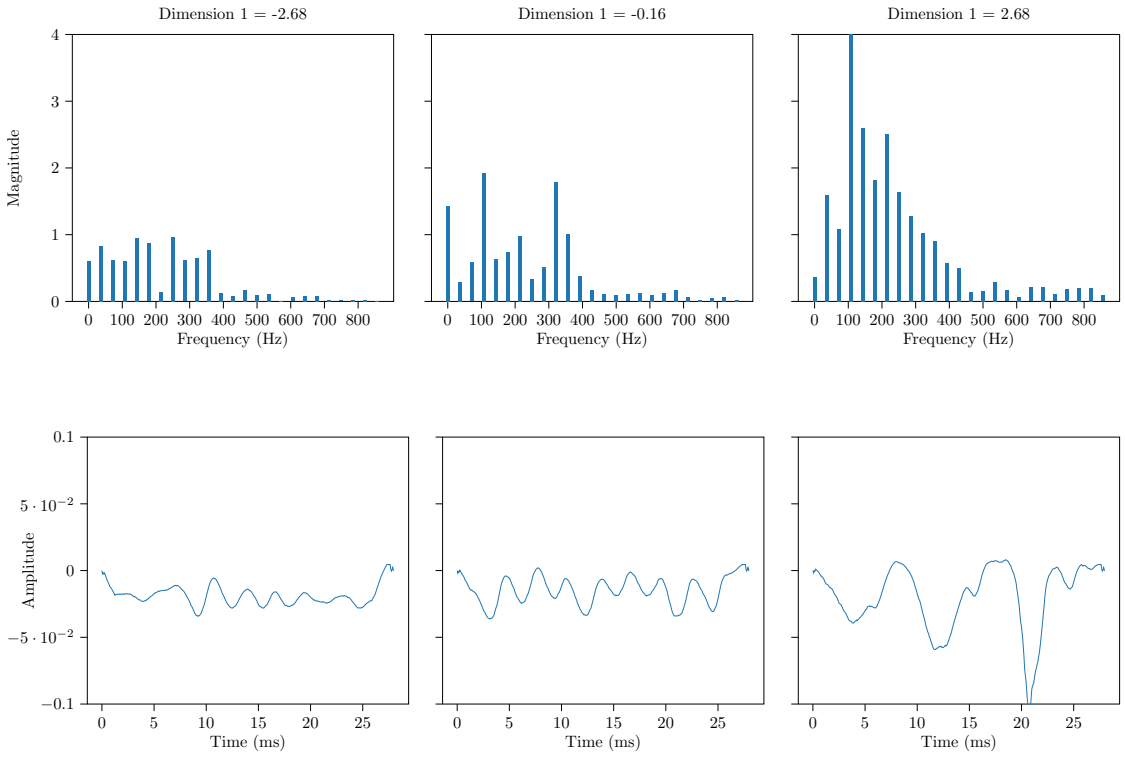

Figure 4.11: Reconstructed speech signal from an *intermediate* latent representation. The first dimension is being modified, while other dimensions are fixed at 0. The dimension has influence on the 150 Hz frequency band, but also neighbouring frequencies.

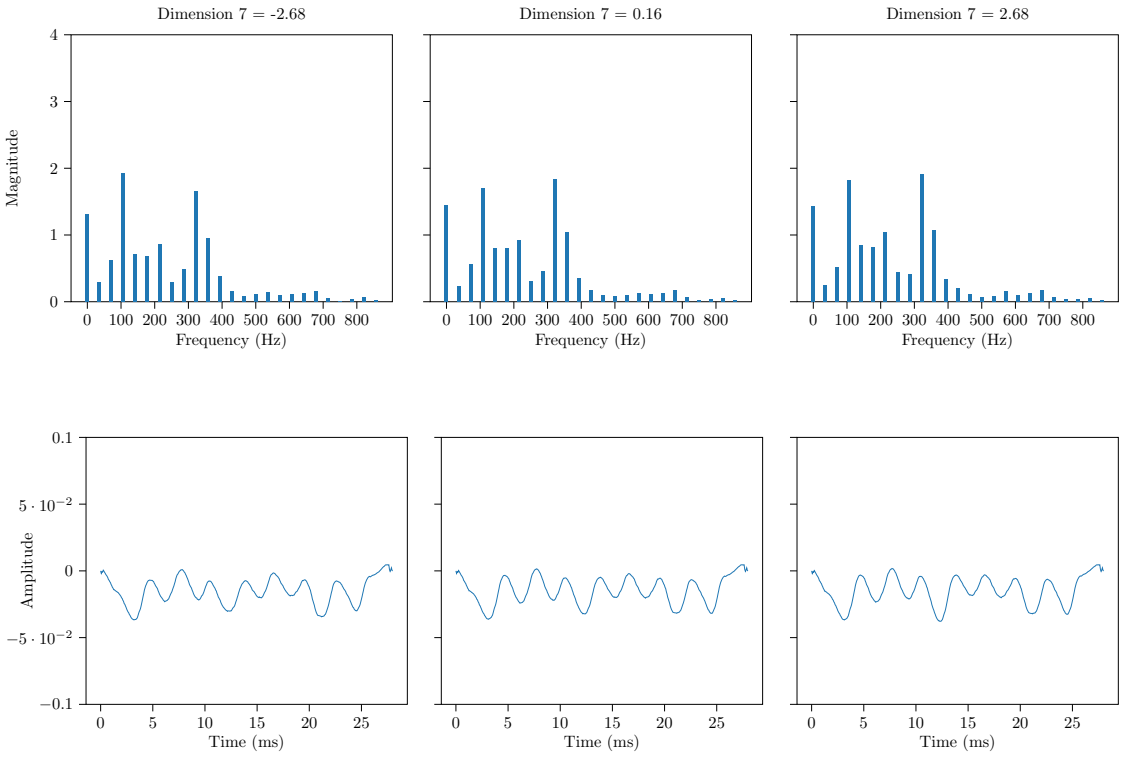

Figure 4.12: Reconstructed speech signal from an *intermediate* latent representation. The seventh dimension is being modified, while other dimensions are fixed at 0. We observe no significant differences when adjusting its corresponding value, indicating that the dimension may not capture any information at all.

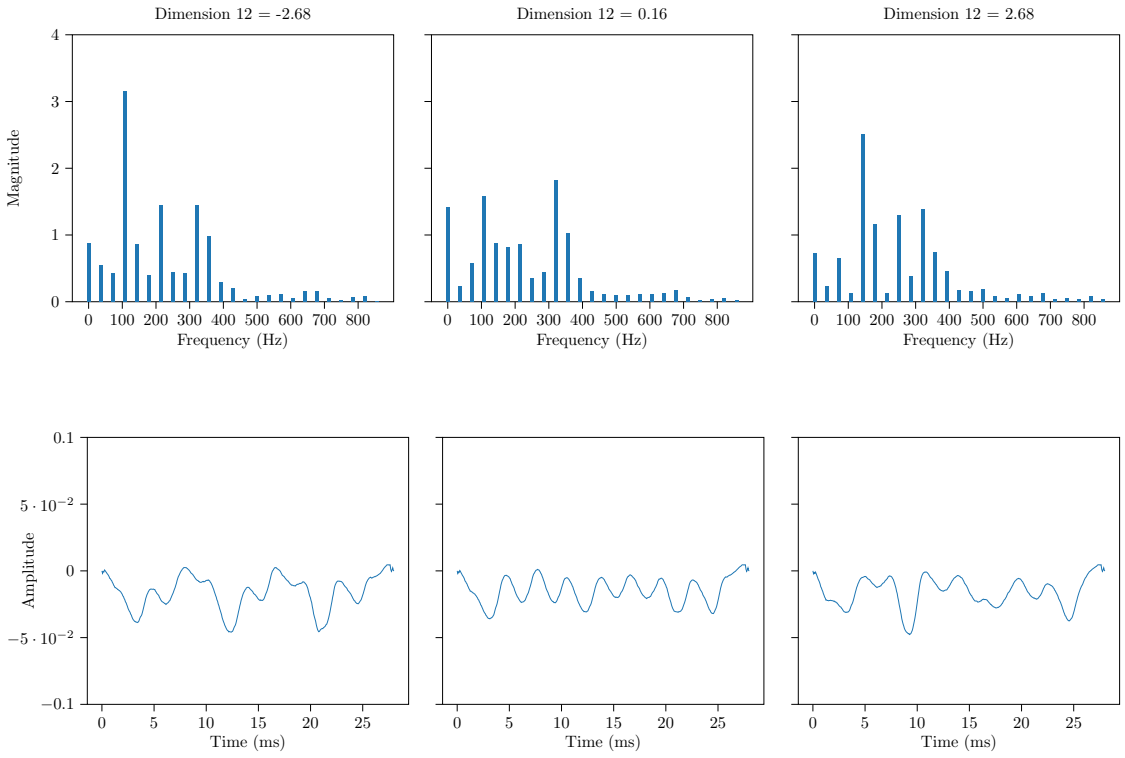

Figure 4.13: Reconstructed speech signal from an *intermediate* latent representation. The twelfth dimension is being modified, while other dimensions are fixed at 0. Negative values cause a large spike around 100 Hz while positive values fully remove the 100Hz and influences the 150Hz range instead.

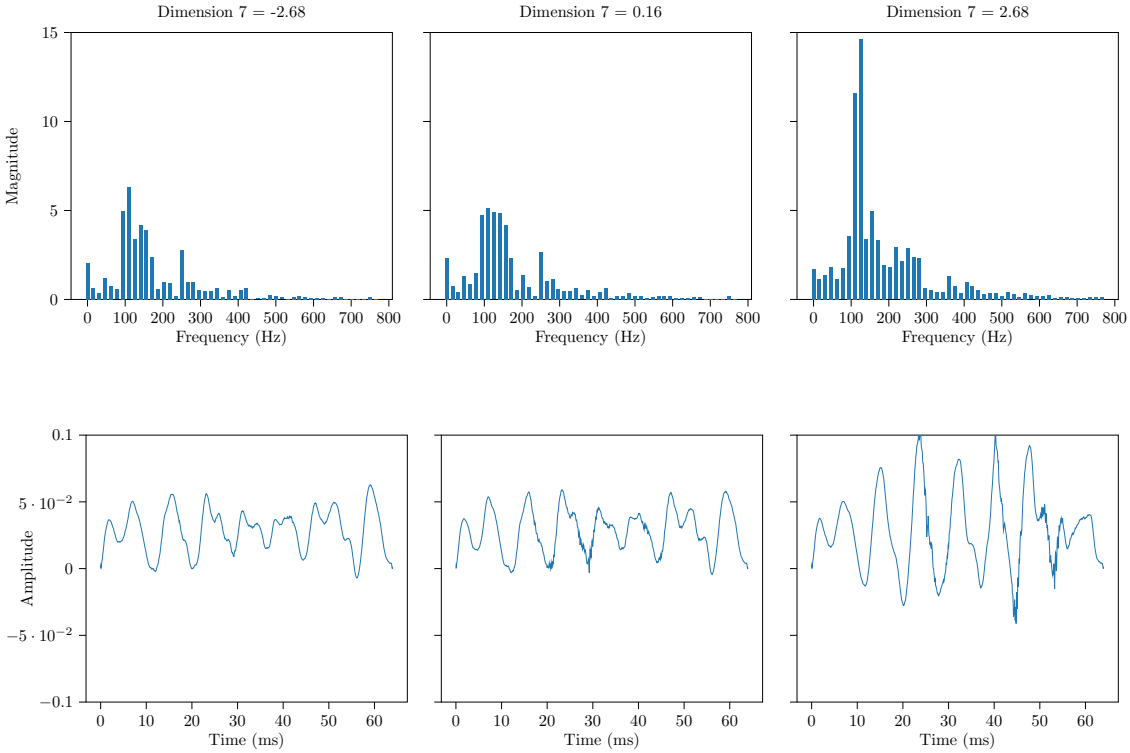

Figure 4.14: Reconstructed speech signal from a *final* latent representation. The seventh dimension is being modified, while other dimensions are fixed at 0. The dimension has influence on the 125 Hz frequency band, but also neighbouring ranges. The magnitudes are also higher.

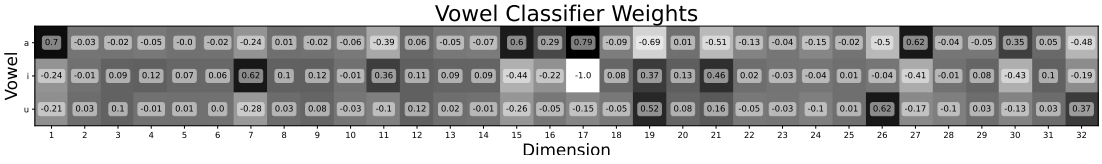

Figure 4.15: Visualisation of weights in the linear vowel classifier. Latent representations from V-GIM's first module are used. The classifier is trained without bias terms.

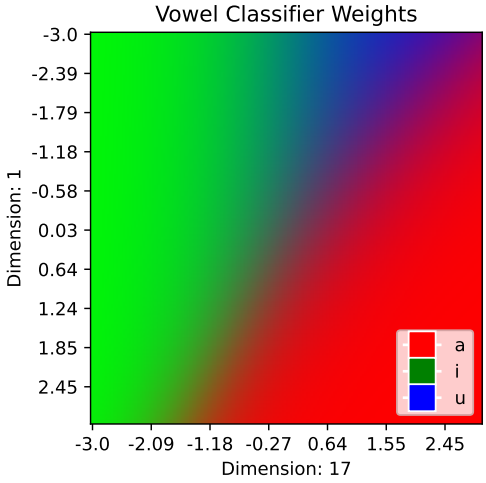

Figure 4.16: Decision boundary in V-GIM's latent space where dimension 1 and 17 are being perturbed while the other dimensions remain fixed at 0.

Chapter 5

Relation to Existing Work

We have studied the representations obtained by optimising the InfoNCE loss function. Through the addition of a regularisation term to the loss, we could analyse the underlying information contained in the representations using a decoder. In this chapter, we give an overview of the existing literature that is relevant to our research. We begin with a discussion on the more recent representation learning techniques related to mutual information (MI) maximisation. We give a non-comprehensive overview of the existing regularisation techniques used for both improved generalisation and better representations. We give an overview of alternative priors that have been introduced to the VAE framework in the past decade. Finally, we conclude this chapter with an overview of the well-known post-hoc explainability techniques and compare them against V-GIM's decoder.

5.1 Representation learning with Mutual Information Maximisation

V-GIM builds upon the concepts of MI maximisation introduced in CPC (van den Oord et al., 2019). It aims to maximise the MI between temporally nearby patches, assuming shared information between nearby data. It is based on the ideas of MI maximisation introduced in CPC and GIM (Löwe et al., 2020; van den Oord et al., 2019). However, MI is notoriously difficult to compute directly and is therefore frequently estimated instead (Tschannen et al., 2020). Poole et al. (2019) provide a taxonomy on this matter. V-GIM, similar to GIM optimises for the InfoNCE bound, which is a lower bound on mutual information (van den Oord et al., 2019). Different approaches also aim to learn representations through MI maximisation. Deep InfoMax (DIM) (Hjelm et al., 2019) incorporates an ANN encoder which maximises the MI between input and output. This is achieved by incorporating knowledge about locality in the representations, resulting in locally-consistent information across structural locations. DIM deals with MI's intractability by using Mutual Information Neural Estimation (MINE) (Belghazi et al., 2021), which offers a MI lower bound based on the Donsker-Varadhan representation (Donsker and Varadhan, 1976).

In contrast, InfoGAN (Chen et al., 2016) takes a variational approach to estimate MI directly. It chooses an approximate posterior from which MI can be approximated. The MI estimation is then incorporated as a regularisation term in a GAN-like loss function, resulting in interpretable representations that influence individual aspects of the generated data. InfoGAN's generator, similar to V-GIM, aims for interpretability using an optional decoder. However, V-GIM goes

further by dividing its architecture into modules, each with their own interpretable representations. This approach enables understanding not only the final representations but also the internal components of the neural network, providing increased interpretability.

Another approach, called Contrastively Disentangled Sequential Variational Autoencoder (C-DSVAE) (Bai et al., 2021), also employs a contrastive method to estimate a lower bound for MI. Similarly to CPC's contrastive approach utilising the InfoNCE bound, C-DSVAE aims to find a lower bound on MI by distinguishing positive samples from negative samples. However, C-DSVAE takes a different approach by using alternative positive and negative samples, allowing it to extract both time-invariant and time-variant factors in the latent representations. This differs from CPC, which uses future data patches as positive samples and random patches as negative samples, relying on the assumption of shared information between nearby data. Like V-GIM, C-DSVAE is designed for sequential data. However, V-GIM does not require a decoder for training. In C-DSVAE, the objective function optimises the log-likelihood (or reconstruction error) introduced in VAEs, and the contrastive estimate of MI is considered an additional regularisation term. In contrast, V-GIM treats MI maximisation as the main learning objective, with KL-divergence used as a regularisation term.

5.2 Regularisation

The practice of adding a penalty term to the loss function, known as regularisation, has been widely used for various purposes. Kukačka et al. (2017) provide a survey and group the regularisation terms in different categories, including those that impose constraints on the weights, or on the activations. V-GIM belongs to the second category, applying constraints to the activations in different layers of the network.

Regularisation terms that enforce constraints on the weights typically aim to improve generalisation performance by penalising complexity. Weight decay, for example, achieves this by applying the L^2-norm on the network weights, encouraging smaller weights (Gnecco and Sanguineti, 2009). Another approach described by Kukačka et al. (2017) is weight smoothing which applies L^2-norm to the gradients during training. Weight elimination is similar to weight decay but favours sparse networks (Weigend et al., 1990). Soft weight-sharing clusters weights together, ensuring that weights within a cluster have similar values (Nowlan and Hinton, 1992).

Tian and Zhang (2022) discuss sparse vector-based regularisation, which imposes constraints on the activations, encouraging activations to approximate zero. This is useful for applications that require sparse representations, such as data compression. Continuing in the line of activation regularisation, Tomczak (2016) introduces a regularisation term that encourages activations to maximise entropy, resulting in uncorrelated and disentangled representations. Meanwhile, Wu et al. (2018) introduce a regularisation term that puts constraints on the output activations to improve the interpretability of representations. In different work, Wu et al. (2021) propose a different approach to improve the interpretability of ANNs. This is achieved by constraining the depth required to approximate the model through a decision tree. The depth of the equivalent decision tree is added as a regularisation term to the loss function. Similarly to V-GIM, Wu et al. aims to achieve better interpretability through an additional regularisation term while maintaining the original objective of the model. However, this approach is limited by the modelling capabilities of decision trees, as it can only be applied to supervised tasks. Consequently, it cannot be used for generative modelling or representation learning. Additionally, it is not well-suited for computer vision problems or speech recognition, as these tasks are difficult to model using decision trees (Stanford MedAI, 2022). Meanwhile, V-GIM does not suffer from these issues.

5.3 Alternative Priors and Posteriors in VAEs

Taking inspiration from VAEs, V-GIM minimises the KL-divergence between the posterior distributions and a fixed prior $p(\mathbf{z}) = \mathcal{N}(\mathbf{0}, \mathbf{I})$. This results in a latent space that can be better understood. However, other possibilities have been suggested in the literature on VAEs concerning different priors or posteriors.

In VAEs, the posterior $q(\mathbf{z} \mid \mathbf{x}^{(i)})$ serves as an approximation to the true posterior $p(\mathbf{z} \mid \mathbf{x}^{(i)})$ (Odaibo, 2019). This approximate posterior is most commonly chosen as a simple factorised Gaussian for mathematical convenience. However, this is often an oversimplification of the true posterior (Nalisnick et al., 2016). Kingma and Welling (2019) demonstrate that the approximate posterior can be extended to a Gaussian with a full covariance matrix. Additionally, Nalisnick et al. (2016) propose a Gaussian mixture model, which combines several Gaussians, as an approximate posterior, enabling the modelling of multimodal posterior distributions.

Continuing in the exploration of Gaussian mixture models, alternative priors have also been investigated. Guo et al. (2020) and Lee et al. (2021) experiment with Gaussian mixture model priors, resulting in improved performance. Additionally, Tomczak and Welling (2018) introduce VampPrior, choosing the prior as a mixture of Gaussian posteriors. This approach improves performance and mitigates issues related to useless dimensions, which is a well-known problem in VAEs and is also observed in V-GIM (see section 4.4.2). In section 6.1, we make recommendations for future work on how these alternative priors or posteriors can be incorporated into V-GIM to deal with these useless dimensions.

5.4 Post-Hoc Explainability

Black-box models (including ANNs) are limited by their lack of interpretability. Consequently, different post-host approaches have been introduced, which aim to explain the predictions these models make. These approaches can be categorised as "model-agnostic", which find explanations irrespective of the model type, or "model-specific", which make assumptions about the underlying workings of the model, for instance by analysing the activations of a neural network Barredo Arrieta et al. (2020).

Two well-known agnostic model approaches are Local Interpretable Model-Agnostic Explanations (LIME) and SHapley Additive exPlanations (SHAP) (Ribeiro et al., 2016; Lundberg and Lee, 2017). These approaches aim to explain individual predictions by assigning a positive or negative contribution score to each input feature with respect to the output prediction (Lundberg and Lee, 2017; Molnar, 2022). High contribution scores indicate features that have a significant impact, enabling humans to analyse which features the model found important. LIME determines its relevance scores by training an interpretable model that approximates the original model. The interpretable model is trained with predictions from the original model around a particular data point (Ribeiro et al., 2016). The interpretable model can for instance be a decision tree (Molnar, 2022). Meanwhile, SHAP obtains its contribution scores based on the Shapely values from coalitional game theory. This enables global interpretation based on the aggregation of the Shapely values (Molnar, 2022).

While model-agnostic approaches do not make assumptions on the black-box model, model-specific approaches do, and can therefore exploit more information resulting in more efficient and potentially more accurate explanations. Saliency maps, also known under the names: pixel attribution maps and sensitivity maps, similar to SHAP and LIME are used to obtain a correspondence score for each input feature (Molnar, 2022). In particular, for convolutional neural networks, Simonyan et al. (2014) obtain the relevance scores by computing a gradient of the predicted class with respect to the input features (or in their case pixels). The result is a series of

partial derivatives, indicating how much the class score will increase (or decrease) given changes to its respective pixel. From this gradient, a saliency map or heatmap can be constructed highlighting the important areas that led to a decision. This idea has also been introduced under the name of Grad-CAM (Selvaraju et al., 2020).

Erhan et al. (2009) and Simonyan et al. (2014) suggest using gradient ascent to find the image that maximally activates a particular neuron, or output class, respectively. V-GIM's decoder can achieve a similar result without needing to apply gradient ascent for each neuron. After the decoder has converged, a latent representation with a maximum activation can be inserted in the decoder of which the original image can be directly decoded. In addition, since V-GIM constraints the latent space to be standard normal it is known up front what the expected range of activations is. The space constraints also ensure that the generated data is more likely to result in data points similar to the dataset, which are potentially easier to analyse. This is different from the results in Erhan et al. (2009); Simonyan et al. (2014), where it is not always clear what is shown in the images as the models were trained without additional regularisation terms.

Chapter 6

Conclusion and Future work

In this thesis, we introduced V-GIM, a self-supervised approach for interpretable representation learning using mutual information (MI) maximisation. In this chapter, we provide a discussion of V-GIM's results with respect to its interpretability. We discuss its limitations and make recommendations for plausible future work. Finally, we conclude this thesis with a summary of our main findings.

6.1 Representation analysis

We analysed V-GIM's representations using t-SNE plots, linear classifiers, and decoders trained on top of V-GIM's representations. We observed that the representations contained vowel information but lacked consonant information. This was observed in both the t-SNE plots and the linear classifier results (see sections 4.2.2 and 4.2.3, respectively). We suggest that this is related to the duration of the phonemes. The InfoNCE objective, from which our loss function is derived, maximises the MI between temporally nearby patches, assuming the presence of common information in nearby data. However, the vowels in the dataset are typically pronounced for longer duration than the consonants, and thus, representations where a consonant is being pronounced have less information in common with nearby representations, as in those representations the consonant may not be pronounced any more. These findings align with Löwe et al. (2020) who suggested that optimisation of the InfoNCE objective favours global information over local information.

The decoder provided insights into the speech information that remained in the representations. While the pronounced sounds were generally recognisable, the decoder occasionally generated incorrect consonants, for instance by producing the sound "ba" when the original sound was "ga". This further supports our findings that the representations contain less consonant information. Additionally, the pronounced sounds were recognisable but sounded distorted. It seemed that information that was not related to the identity of phonemes (for instance related to the identity of the speaker) was almost entirely lost. This suggests that (among others) features needed for speaker identification may no longer be present in the representations.

Interestingly, the vowel information was found to be concentrated in only a small subset of dimensions. This was observed in the vowel experiment, where a linear classifier trained on V-GIM's first module achieved high accuracies by assigning high weights to a few dimensions, while the majority of weights were close to zero, indicating that those dimensions did not contribute to the prediction. This suggests that the size of representations could be further reduced by

removing dimensions that did not contribute to the task. Some of these dimensions likely carry different information, while others may be completely useless.

We attribute the presence of useless dimensions in V-GIM's representations to the KL divergence term in the $\mathcal{L}_{\text{V-NCE}}$ loss function (see section 3.3). The histogram plots (see section 4.2.4) revealed that some dimensions' distributions were nearly identical to the standard normal distribution, while others showed more variation. We assume that the dimensions with more variation most likely carry all the actual information and contribute to a good InfoNCE bound, while the identical dimensions do not carry any useful information but help maintain a low KL divergence.

This problem of useless dimensions is also known in VAEs and can be mitigated by choosing different priors or posteriors. For instance, VampPrior addresses this problem by using a mixture of Gaussians as prior instead of the typical standard normal (Tomczak and Welling, 2018). Further work could explore alternative priors introduced to VAEs which we discussed in section 5.3, and investigate their performance in V-GIM. Alternatively, the problem of useless dimensions could potentially be mitigated by introducing a regularisation term applied to the weights of the similarity score function $f_k^m(\mathbf{z}_{t+k}^m, \mathbf{z}_t^m)$, which would enforce similar weights between different dimensions. This regularisation would encourage each dimension to contribute an equal amount of information.

With regards to representation disentanglement, Burgess et al. (2018) argue that choosing a standard normal prior in VAEs encourages disentangled representations. Similarly, V-GIM also utilises a standard normal prior, and its impact concerning disentanglement should be further investigated in future work.

Continuing with the interpretability analysis, V-GIM's regularisation term ensures that sampling a random point in the latent space around the origin will likely result in a point that is similar to the original data. Since the training set covers the entire space around the origin, a decoder trained on this space will likely generalise well to unseen data around the origin. Therefore, the interpolation experiment allowed us to investigate what exact information was contained in each dimension in each of V-GIM's modules. We discovered three categories: dimensions containing information from one or two specific frequency bins, dimensions containing information spanning a range of frequency bins, and dimensions containing no information at all. Most dimensions were active around the 100 Hz to 200 Hz frequency range, similar to the pitch of a male voice (Re et al., 2012).

While our work focused on understanding V-GIM's representations for two modules, achieving true explainable AI requires understanding not only the model's outputs but also how it obtained its outputs. V-GIM could serve as an initial step in this direction by defining each layer as a module, allowing for a better understanding of each activation in the network. Further research could explore the associated weights between modules to gain further insights into the model's internal workings.

6.2 Performance and Other Applications

The syllable classifier (see section 4.2.3) provided insights into V-GIM's performance, which we compared to GIM. Overall, V-GIM's performance is similar to GIM, indicating that the additional regularisation term resulting in better interpretable representations, does not harm performance significantly.

However, results were mediocre for both GIM and V-GIM, obtaining test accuracies around 51% and 54% for the nine classes, with performance further decreasing in the deeper modules. Meanwhile, van den Oord et al. (2019) and Löwe et al. (2020) observed better performance in their

papers for a similar speech recognition problem, for phoneme classification on the LibriSpeech dataset. In particular, Löwe et al. obtained an accuracy of 73.4% with GIM and 64.9% with CPC.

We attribute this performance discrepancy to the captured speech duration that each representation captures. Löwe et al. and van den Oord et al. make use of the same architecture where representations capture smaller speech durations compared to our architecture. Their representations must thus summarise shorter time frames, while also having more capacity to do so, having a total of 512 dimensions per representation rather than 32 as is in our case. As our primary focus was to understand the models underlying representations, rather than obtain state-of-the-art performance, we accepted this loss in performance.

In addition to the more restricted capacity of our representations, the nature of the sequential data also plays a major role in the performance. In particular, MI maximising using the InfoNCE objective requires the presence of common information between the temporally nearby patches of data. However, as the window length increases of individual representations in the deeper convolutional layers, there may be less common information in the nearby patches for the InfoNCE objective to capitalise on. For instance, consider a speech wave where the syllable "ba" is being pronounced. This syllable contains two building blocks, the "b" and the "a". If this syllable would be represented by exactly two representations, one representation capturing the time window where the "b" is being pronounced, and the second for the "a", then these windows no longer have the same pronounced phoneme in common. Consequently, since the InfoNCE objective aims to preserve the common information between these windows and considers inconsistencies as noise, their representations will no longer contain information on the pronounced phoneme. This is observed in the decreased performance of the deeper modules, where deeper representations must encode longer speech windows. The extent to which sequential data can be downscaled is thus dependent on the amount of MI between the patches.

While performance decreases in the deeper modules due to limited MI, V-GIM significantly outperforms GIM in the syllable experiment within the second module. V-GIM achieves a test accuracy of 42%, compared to GIM's 30% (see section 4.2.3). We hypothesise this is related to V-GIM's internal batch normalisation mechanism between modules, thus preventing internal covariate shift from occurring between modules. Meanwhile, GIM does not have any normalisation in between modules, resulting in successive modules not being able to catch up with the changes from the predeceasing modules. While this problem did not become apparent for Löwe et al., we argue that this is related to the smaller learning rate and restricted architecture depths which consist of a single layer per module, and thus is less punished by internal covariate shift.

Furthermore, V-GIM's representation variability could potentially provide a generalisation benefit for downstream tasks when little labelled data is available, as the distributions limit the number of plausible decision boundaries that can separate the data. However, the linear classifiers trained on a smaller subset of the labelled data did not seem to benefit from this variability and obtained similar performance to those trained with GIM's representations (see section 4.3).

One hypothesis is that the classifiers are optimised using the cross entropy loss function and therefore, may behave similarly to Support Vector Machines (SVM). SVMs can filter out a large amount of the plausible decision boundaries by selecting the boundary that maximises the margin between the classes (Hearst et al., 1998; Noble, 2006). As a result, V-GIM's restrictions on the number of decision boundaries do not make a significant contribution to better generalisation, as many potential decision boundaries that would separate the data are already eliminated. At this moment, this is only a conjecture and should be investigated more thoroughly in future work. Additionally, alternative downstream tasks learned with V-GIM's representations should be investigated as well. Different learning algorithms such as the Perceptron Learning Algo-

rithm (PLA) could potentially find better value in V-GIM's representations compared to GIM's representations. These findings would not only be interesting for V-GIM but also for VAEs.

Another interesting research line would be in quantised learning, which aims to make ANNs more efficient and less memory expensive by making use of reduced-precision representations for the weights and activations in the network Blott et al. (2018). However, this reduced precision results in more zero gradients as gradients approaching zero have less precision to differentiate themselves from an actual value of zero. Quantised learning is therefore even more susceptible to the vanishing gradient problem (Kim et al., 2021). V-GIM could potentially provide a solution to this problem. In V-GIM, modules are trained greedily and gradients do not flow between modules. This makes V-GIM less prone to vanishing gradients, as discussed by Löwe et al. (2020). Future work should investigate quantised learning with V-GIM further, as it could offer a solution to obtain the benefits from quantised learning without being affected by the drawbacks.

Finally, V-GIM's regularisation term pulls data points in the latent space close to the centre. The distance from the origin could potentially be used as a reliability score. For example, when V-GIM applies inference on new data, values far from the centre could potentially be flagged as outliers, providing indications of data that the model cannot generalise well to. Future work could incorporate this information using outlier detectors, offering solutions for continuous training methodologies in a production environment.

6.3 Final Conclusion

We have introduced Variational Greedy InfoMax (V-GIM), a self-supervised representation learning approach which incorporates interpretability requirements into the design of the model. V-GIM builds upon the greedy layer-wise learning approach of GIM, benefiting from decoupled and asynchronous distributed training while addressing the vanishing gradient problem. Additionally, V-GIM benefits from VAEs' disentangled representations and representation variability.

By applying constraints to the latent space of each module, V-GIM's greedy learning approach results in an internal batch normalisation mechanism. This mechanism, leads to improved performance of the deeper modules, outperforming V-GIM's non-variational counterpart, GIM. However, the representation variability obtained from V-GIM's stochastic representations does not appear to improve the performance of downstream tasks in scenarios where labelled data is scarce. Future work should investigate this in more detail, as these findings could potentially be attributed to the nature of the downstream task rather than the quality of the representations themselves.

V-GIM's improved interpretability is achieved through its ability to analyse internal representations using a decoder. By imposing latent space constraints, V-GIM ensures meaningful decodings that provide valuable insights into the underlying structure of these representations, which is not the case in GIM. We found that V-GIM learned internal representations which were sensitive to specific vowels, while consonant information was lacking. Furthermore, individual dimensions in the representations captured information on specific frequency bins or entire neighbourhoods of frequency bins. Meanwhile, certain dimensions did not appear to contain any information at all. This shows that the individual concepts that neurons are sensitive to, can be observed for both the output and internal neurons, thus allowing us to gain a deeper understanding of the internal mechanisms learned by these networks. Consequently, this brings us one step closer to comprehending the complex workings of neural networks.

Bibliography

Ackley, D. H., Hinton, G. E., and Sejnowski, T. J. (1985). A learning algorithm for boltzmann machines. *Cognitive Science*, 9(1):147–169.

Alammar, J. (2021). Explainable AI Guide. https://ex.pegg.io/.

Bai, J., Wang, W., and Gomes, C. P. (2021). Contrastively Disentangled Sequential Variational Autoencoder. In *Advances in Neural Information Processing Systems*, volume 34, pages 10105–10118. Curran Associates, Inc.

Bank, D., Koenigstein, N., and Giryes, R. (2021). Autoencoders.

Barbiero, P., Squillero, G., and Tonda, A. (2020). Modeling Generalization in Machine Learning: A Methodological and Computational Study.

Barredo Arrieta, A., Díaz-Rodríguez, N., Del Ser, J., Bennetot, A., Tabik, S., Barbado, A., Garcia, S., Gil-Lopez, S., Molina, D., Benjamins, R., Chatila, R., and Herrera, F. (2020). Explainable Artificial Intelligence (XAI): Concepts, taxonomies, opportunities and challenges toward responsible AI. *Information Fusion*, 58:82–115.

Bau, D., Zhou, B., Khosla, A., Oliva, A., and Torralba, A. (2017). Network Dissection: Quantifying Interpretability of Deep Visual Representations.

Belghazi, M. I., Baratin, A., Rajeswar, S., Ozair, S., Bengio, Y., Courville, A., and Hjelm, R. D. (2021). MINE: Mutual Information Neural Estimation.

Bengio, Y., Courville, A., and Vincent, P. (2013). Representation Learning: A Review and New Perspectives. *IEEE transactions on pattern analysis and machine intelligence*, 35:1798–1828.

Bhandari, P. (2020). The Standard Normal Distribution — Calculator, Examples & Uses. https://www.scribbr.com/statistics/standard-normal-distribution/.

Bhargav Lad (2020). Guide to Pytorch Learning Rate Scheduling. https://kaggle.com/code/isbhargav/guide-to-pytorch-learning-rate-scheduling.

Bhati, S., Villalba, J., Żelasko, P., Moro-Velazquez, L., and Dehak, N. (2021). Segmental Contrastive Predictive Coding for Unsupervised Word Segmentation.

Bindu, H. and Prasad, K. (2012). An Efficient Medical Image Segmentation Using Conventional OTSU Method. *International Journal of Advanced Science and Technology*, 38.

Bjorck, N., Gomes, C. P., Selman, B., and Weinberger, K. Q. (2018). Understanding Batch Normalization. In *Advances in Neural Information Processing Systems*, volume 31. Curran Associates, Inc.

Blott, M., Preußer, T. B., Fraser, N. J., Gambardella, G., O'brien, K., Umuroglu, Y., Leeser, M., and Vissers, K. (2018). FINN-R: An End-to-End Deep-Learning Framework for Fast Exploration of Quantized Neural Networks. *ACM Transactions on Reconfigurable Technology and Systems*, 11(3):16:1–16:23.

Braun, S. and Tashev, I. (2020). A consolidated view of loss functions for supervised deep learning-based speech enhancement.

Burgess, C. P., Higgins, I., Pal, A., Matthey, L., Watters, N., Desjardins, G., and Lerchner, A. (2018). Understanding disentangling in β-VAE.

Chen, T., Kornblith, S., Norouzi, M., and Hinton, G. (2020). A Simple Framework for Contrastive Learning of Visual Representations.

Chen, X., Duan, Y., Houthooft, R., Schulman, J., Sutskever, I., and Abbeel, P. (2016). InfoGAN: Interpretable Representation Learning by Information Maximizing Generative Adversarial Nets.

Chung, Y., Haas, P. J., Upfal, E., and Kraska, T. (2019). Unknown Examples & Machine Learning Model Generalization.

Cinelli, L. P., Marins, M. A., Barros da Silva, E. A., and Netto, S. L. (2021). *Variational Methods for Machine Learning with Applications to Deep Networks*. Springer International Publishing, Cham, 1st ed. 2021 edition edition.

Cover, T. M. and Thomas, J. A. (2006). *Elements of Information Theory 2nd Edition*. Wiley-Interscience, Hoboken, N.J, 2nd edition edition.

Data Science Courses (2017). Ali Ghodsi, Lec : Deep Learning, Variational Autoencoder, Oct 12 2017 [Lect 6.2].

David Foster (2023). 3. Variational Autoencoders. In *Generative Deep Learning, 2nd Edition*. O'Reilly Media, Inc., second edition.

de Haan, P. and Löwe, S. (2021). Contrastive Predictive Coding for Anomaly Detection.

Deldari, S., Smith, D. V., Xue, H., and Salim, F. D. (2021). Time Series Change Point Detection with Self-Supervised Contrastive Predictive Coding. In *Proceedings of the Web Conference 2021*, WWW '21, pages 3124–3135, New York, NY, USA. Association for Computing Machinery.

Doersch, C. (2021). Tutorial on Variational Autoencoders.

Donsker, M. D. and Varadhan, S. R. S. (1976). Asymptotic evaluation of certain Markov process expectations for large time—III. In *Communications on Pure and Applied Mathematics*, volume 29, pages 389–461.

Erhan, D., Bengio, Y., Courville, A., and Vincent, P. (2009). Visualizing Higher-Layer Features of a Deep Network. *Technical Report, Univeristé de Montréal*.

Fu, M. C. (2016). AlphaGo and Monte Carlo tree search: The simulation optimization perspective. In *2016 Winter Simulation Conference (WSC)*, pages 659–670.

Gnecco, G. and Sanguineti, M. (2009). The weight-decay technique in learning from data: An optimization point of view. *Computational Management Science*, 6:53–79.

Grossutti, M., D'Amico, J., Quintal, J., MacFarlane, H., Quirk, A., and Dutcher, J. R. (2022). Deep Learning and Infrared Spectroscopy: Representation Learning with a Beta-Variational Autoencoder. *The Journal of Physical Chemistry Letters*, 13(25):5787–5793.

Guo, C., Zhou, J., Chen, H., Ying, N., Zhang, J., and Zhou, D. (2020). Variational Autoencoder With Optimizing Gaussian Mixture Model Priors. *IEEE Access*, 8:43992–44005.

Hearst, M., Dumais, S., Osuna, E., Platt, J., and Scholkopf, B. (1998). Support vector machines. *IEEE Intelligent Systems and their Applications*, 13(4):18–28.

Henaff, O. (2020). Data-Efficient Image Recognition with Contrastive Predictive Coding. In *Proceedings of the 37th International Conference on Machine Learning*, pages 4182–4192. PMLR.

Higgins, I., Matthey, L., Pal, A., Burgess, C., Glorot, X., Botvinick, M., Mohamed, S., and Lerchner, A. (2022). Beta-VAE: Learning Basic Visual Concepts with a Constrained Variational Framework. In *International Conference on Learning Representations*.

Hjelm, R. D., Fedorov, A., Lavoie-Marchildon, S., Grewal, K., Bachman, P., Trischler, A., and Bengio, Y. (2019). Learning deep representations by mutual information estimation and maximization.

Ho, Y. and Wookey, S. (2020). The Real-World-Weight Cross-Entropy Loss Function: Modeling the Costs of Mislabeling. *IEEE Access*, 8:4806–4813.

Hu, Z., Zhang, J., and Ge, Y. (2021). Handling Vanishing Gradient Problem Using Artificial Derivative. *IEEE Access*, 9:22371–22377.

Ioffe, S. and Szegedy, C. (2015). Batch Normalization: Accelerating Deep Network Training by Reducing Internal Covariate Shift.

Jain, A., Mao, J., and Mohiuddin, K. (1996). Artificial neural networks: A tutorial. *Computer*, 29(3):31–44.

Karagiannakos, S. (2018). How to Generate Images using Autoencoders. https://theaisummer.com/Autoencoder/.

Kim, D., Lee, J., and Ham, B. (2021). Distance-aware Quantization.

Kingma, D. P. and Welling, M. (2019). An Introduction to Variational Autoencoders. *Foundations and Trends® in Machine Learning*, 12(4):307–392.

Kingma, D. P. and Welling, M. (2022). Auto-Encoding Variational Bayes.

Krizhevsky, A., Sutskever, I., and Hinton, G. E. (2012). ImageNet classification with deep convolutional neural networks. In Pereira, F., Burges, C., Bottou, L., and Weinberger, K., editors, *Advances in Neural Information Processing Systems*, volume 25. Curran Associates, Inc.

Krogh, A. (2008). What are artificial neural networks? *Nature Biotechnology*, 26(2):195–197.

Krug, A., Ebrahimzadeh, M., Alemann, J., Johannsmeier, J., and Stober, S. (2021). Analyzing and Visualizing Deep Neural Networks for Speech Recognition with Saliency-Adjusted Neuron Activation Profiles. *Electronics*, 10(11):1350.

Kukačka, J., Golkov, V., and Cremers, D. (2017). Regularization for Deep Learning: A Taxonomy.

Le-Khac, P. H., Healy, G., and Smeaton, A. F. (2020). Contrastive Representation Learning: A Framework and Review. *IEEE Access*, 8:193907–193934.

Lecun, Y., Bottou, L., Bengio, Y., and Haffner, P. (1998). Gradient-based learning applied to document recognition. *Proceedings of the IEEE*, 86(11):2278–2324.

LeCun, Y., Bottou, L., Orr, G. B., and Müller, K. R. (1998). Efficient BackProp. In Orr, G. B. and Müller, K.-R., editors, *Neural Networks: Tricks of the Trade*, Lecture Notes in Computer Science, pages 9–50. Springer, Berlin, Heidelberg.

Lee, D. B., Min, D., Lee, S., and Hwang, S. J. (2021). Meta-GMVAE: Mixture of Gaussian VAE for Unsupervised Meta-Learning. In *International Conference on Learning Representations*.

Li, A., Peng, R., Zheng, C., and Li, X. (2020). A Supervised Speech Enhancement Approach with Residual Noise Control for Voice Communication. *Applied Sciences*, 10(8):2894.

Löwe, S., O'Connor, P., and Veeling, B. S. (2020). Putting An End to End-to-End: Gradient-Isolated Learning of Representations.

Lu, M. Y., Chen, R. J., Wang, J., Dillon, D., and Mahmood, F. (2019). Semi-Supervised Histology Classification using Deep Multiple Instance Learning and Contrastive Predictive Coding.

Lucas, J., Tucker, G., Grosse, R., and Norouzi, M. (2022). Understanding Posterior Collapse in Generative Latent Variable Models. *International Conference on Learning Representations*.

Lundberg, S. M. and Lee, S.-I. (2017). A Unified Approach to Interpreting Model Predictions. In *Advances in Neural Information Processing Systems*, volume 30. Curran Associates, Inc.

Marblestone, A. H., Wayne, G., and Kording, K. P. (2016). Toward an Integration of Deep Learning and Neuroscience. *Frontiers in Computational Neuroscience*, 10.

Molnar, C. (2022). *Interpretable Machine Learning: A Guide For Making Black Box Models Explainable*. Independently published, Munich, Germany.

Nalisnick, E. T., Hertel, L., and Smyth, P. (2016). Approximate Inference for Deep Latent Gaussian Mixtures.

Neyshabur, B., Bhojanapalli, S., Mcallester, D., and Srebro, N. (2017). Exploring Generalization in Deep Learning. In *Advances in Neural Information Processing Systems*, volume 30. Curran Associates, Inc.

Noble, W. S. (2006). What is a support vector machine? *Nature Biotechnology*, 24(12):1565–1567.

Nowlan, S. J. and Hinton, G. E. (1992). Simplifying Neural Networks by Soft Weight-Sharing. *Neural Computation*, 4(4):473–493.

Odaibo, S. (2019). Tutorial: Deriving the Standard Variational Autoencoder (VAE) Loss Function.

Otsu, N. (1979). A Threshold Selection Method from Gray-Level Histograms. *Institute of Electrical and Electronics Engineers*.

Paszke, A., Gross, S., Chintala, S., Chanan, G., Yang, E., DeVito, Z., Lin, Z., Desmaison, A., Antiga, L., and Lerer, A. (2017). Automatic differentiation in PyTorch. *Conference on Neural Information Processing Systems*.

Poole, B., Ozair, S., van den Oord, A., Alemi, A. A., and Tucker, G. (2019). On Variational Bounds of Mutual Information.

Przybyszewski, P., Dziewiatkowski, S., Jaszczur, S., Smiech, M., and Szczuka, M. (2017). Use of domain knowledge and feature engineering in helping AI to play Hearthstone. In *2017 Federated Conference on Computer Science and Information Systems (FedCSIS)*, pages 143–148.

Radkoff, E. (2021). Loss Functions in Audio ML. https://soundsandwords.io//audio-loss-functions/.

Rao, S. S. (2020). Understanding the Gradient-Isolated Learning of Representations and intuition to the Greedy. . . .

Re, D. E., O'Connor, J. J. M., Bennett, P. J., and Feinberg, D. R. (2012). Preferences for Very Low and Very High Voice Pitch in Humans. *PLoS ONE*, 7(3):e32719.

Ribeiro, M. T., Singh, S., and Guestrin, C. (2016). "Why Should I Trust You?": Explaining the Predictions of Any Classifier.

Rumelhart, D., Hinton, G., and Williams, R. (1988). Learning Internal Representations by Error Propagation. In *Readings in Cognitive Science*, pages 399–421. Elsevier.

Santurkar, S., Tsipras, D., Ilyas, A., and Madry, A. (2018). How Does Batch Normalization Help Optimization? In *Advances in Neural Information Processing Systems*, volume 31. Curran Associates, Inc.

Selvaraju, R. R., Cogswell, M., Das, A., Vedantam, R., Parikh, D., and Batra, D. (2020). Grad-CAM: Visual Explanations from Deep Networks via Gradient-based Localization. *International Journal of Computer Vision*, 128(2):336–359.

Shah, R. (2020). [AN #92]: Learning good representations with contrastive predictive coding.

Shen, J., Pang, R., Weiss, R. J., Schuster, M., Jaitly, N., Yang, Z., Chen, Z., Zhang, Y., Wang, Y., Skerrv-Ryan, R., Saurous, R. A., Agiomvrgiannakis, Y., and Wu, Y. (2018). Natural TTS Synthesis by Conditioning Wavenet on MEL Spectrogram Predictions. In *2018 IEEE International Conference on Acoustics, Speech and Signal Processing (ICASSP)*, pages 4779–4783.

Sikka, H., Zhong, W., Yin, J., and Pehlevant, C. (2019). A Closer Look at Disentangling in β-VAE. In *2019 53rd Asilomar Conference on Signals, Systems, and Computers*, pages 888–895.

Simonyan, K., Vedaldi, A., and Zisserman, A. (2014). Deep Inside Convolutional Networks: Visualising Image Classification Models and Saliency Maps.

Stacke, K., Lundström, C., Unger, J., and Eilertsen, G. (2020). Evaluation of Contrastive Predictive Coding for Histopathology Applications. In *Proceedings of the Machine Learning for Health NeurIPS Workshop*, pages 328–340. PMLR.

Stanford MedAI (2022). MedAI #34: Optimizing for Interpretability in Deep Neural Networks — Mike Wu.

Teach Wonderful (2021). Let's explore the International Phonetic Alphabet (IPA).

Tian, Y. and Zhang, Y. (2022). A comprehensive survey on regularization strategies in machine learning. *Information Fusion*, 80:146–166.

Tomczak, J. and Welling, M. (2018). VAE with a VampPrior. In *Proceedings of the Twenty-First International Conference on Artificial Intelligence and Statistics*, pages 1214–1223. PMLR.

Tomczak, J. M. (2016). Learning Informative Features from Restricted Boltzmann Machines. *Neural Processing Letters*, 44(3):735–750.

Tschannen, M., Bachem, O., and Lucic, M. (2018). Recent Advances in Autoencoder-Based Representation Learning.

Tschannen, M., Djolonga, J., Rubenstein, P. K., Gelly, S., and Lucic, M. (2020). On Mutual Information Maximization for Representation Learning.

Vali, A., Comai, S., and Matteucci, M. (2020). Deep Learning for Land Use and Land Cover Classification Based on Hyperspectral and Multispectral Earth Observation Data: A Review. *Remote Sensing*, 12(15):2495.

van den Oord, A., Li, Y., and Vinyals, O. (2019). Representation Learning with Contrastive Predictive Coding.

van der Maaten, L. and Hinton, G. (2008). Visualizing Data using t-SNE. *Journal of Machine Learning Research*, 9(86):2579–2605.

Wei, R. and Mahmood, A. (2021). Recent Advances in Variational Autoencoders With Representation Learning for Biomedical Informatics: A Survey. *IEEE Access*, 9:4939–4956.

Wei, W., Hu, X., Liu, H., Zhou, M., and Song, Y. (2021). Towards Integration of Domain Knowledge-Guided Feature Engineering and Deep Feature Learning in Surface Electromyography-Based Hand Movement Recognition. *Computational Intelligence and Neuroscience*, 2021:e4454648.

Weigend, A., Rumelhart, D., and Huberman, B. (1990). Generalization by Weight-Elimination with Application to Forecasting. In *Advances in Neural Information Processing Systems*, volume 3. Morgan-Kaufmann.

Wu, C., Gales, M. J. F., Ragni, A., Karanasou, P., and Sim, K. C. (2018). Improving Interpretability and Regularization in Deep Learning. *IEEE/ACM Transactions on Audio, Speech, and Language Processing*, 26(2):256–265.

Wu, M., Parbhoo, S., Hughes, M. C., Roth, V., and Doshi-Velez, F. (2021). Optimizing for Interpretability in Deep Neural Networks with Tree Regularization. *Journal of Artificial Intelligence Research*, 72:1–37.

Zeiler, M. D. and Fergus, R. (2013). Visualizing and Understanding Convolutional Networks.

Zhang, X., Xing, Y., Sun, K., and Guo, Y. (2021). OmiEmbed: A Unified Multi-Task Deep Learning Framework for Multi-Omics Data. *Cancers*, 13(12):3047.

Zhang, Z. (2018). Artificial Neural Network. In Zhang, Z., editor, *Multivariate Time Series Analysis in Climate and Environmental Research*, pages 1–35. Springer International Publishing, Cham.

Zhang, Z. and Tao, D. (2012). Slow Feature Analysis for Human Action Recognition. *IEEE Transactions on Pattern Analysis and Machine Intelligence*, 34(3):436–450.

Zheng, A. and Casari, A. (2018). *Feature Engineering for Machine Learning: Principles and Techniques for Data Scientists*. "O'Reilly Media, Inc.".

Appendices

Appendix A

Syllable classification through histogram segmentation

The syllable classifiers in sections 4.2.3 and 4.3 take as input a fixed-length speech wave of a syllable. However, the words in the speech dataset are not yet split up into syllables, and we must do this ourselves.

To split up the sound files in the dataset, we make use of Otsu's histogram segmentation algorithm (Otsu, 1979). Afterwards, the split speech waves are padded with zeros in the front and back such that each wave has the same length. The files are padded to contain 8800 samples (at a sample rate of 16 kHz.).

Otsu's algorithm is traditionally used for segmentation applications on greyscale images. Given a single image, it chooses a particular intensity threshold and classifies all pixels into one of two classes depending on whether their intensity values are smaller or larger than the threshold. The threshold is chosen to be the one that minimises the intra-class variance (Bindu and Prasad, 2012).

We explore an alternative domain for the algorithm and use it to find an amplitude threshold in the speech waves. The recordings are consistent in loudness and each file contains exactly three syllables of the form "consonant - vowel". It, therefore, suffices to find a single threshold per audio file that classifies the amplitudes as vowel or consonant.

We first max pool the audio waves with a window size of 0.02 seconds. This emphasises the discrepancy in amplitude between vowels and consonants, as shown in figure A.1b. The threshold that minimises the variance for the two classes is computed using a histogram, shown in figure A.1c, in this case, 0.10.

The time windows with amplitude smaller than 0.10 are classified as consonants and the other time windows as vowels. However, when directly using the threshold on the max pooled speech wave we observed that not all consonants were detected, and thus too much speech wave was being classified as consonant. Instead, we found that applying the threshold (still obtained from the max pooled speech wave) to the 90th percentile was a good compromise between classifying speech chunks as vowels or consonants. Once the vowels and consonants are obtained, syllables are computed at transition points going from vowel to consonant, shown in figure A.1a. The transition points mark the ending of a syllable.

Apart from a few edge cases, this technique worked well enough for our purposes. In the cases where more than three vowels were obtained, the transition points closest to the one-third and two-third duration mark were considered instead.

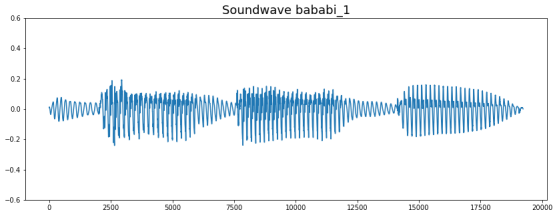

(a) Sound wave for “ba ba bi”, which should be split up into “ba”, “ba and “bi”.

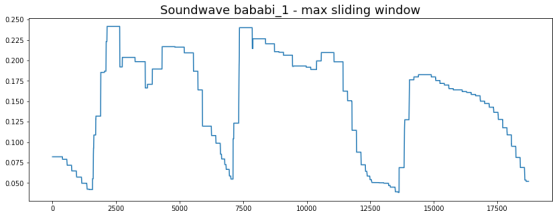

(b) Resulting speech wave after max pooling. The threshold will be computed using this speech wave.

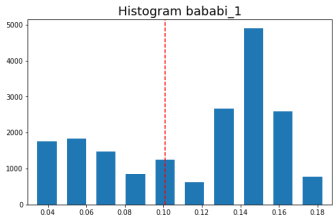

(c) Threshold obtained using Otsu’s algorithm. The red dashed line corresponds to the threshold.

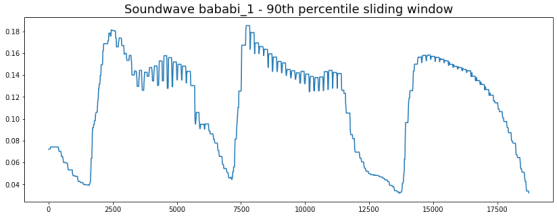

(d) 90’th percentile speech wave (computed using moving window of 0.02 seconds). The threshold is applied to this speech wave. Amplitudes larger than the threshold are considered vowels and smaller values are consonants.

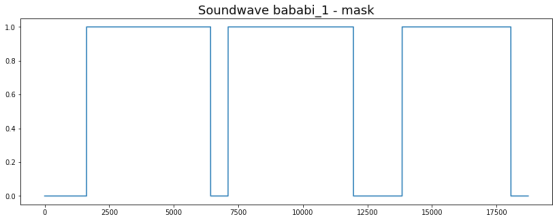

(e) Obtained mask from applying the threshold. The x coordinates going from one to zero are transition points and mark the end of a syllable. There are three potential points in this image. Since each audio file contains three syllables (and thus a maximum of two transition points), the two *true* points are selected based on their distance from the one-third and two-third x coordinate. In this case, the last transition point will be discarded.

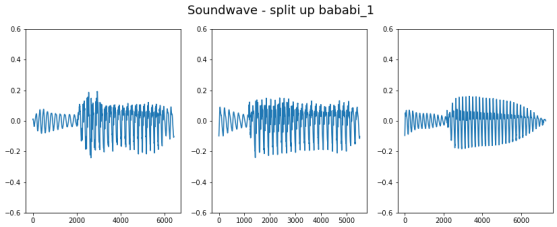

(f) The three obtained syllables after cutting the speech wave at the two transition points.